Structures 69 (2024) 107248

Contents lists available at ScienceDirect

Structures

journal homepage: www.elsevier.com/locate/structures

Simulation and prediction of residual stresses in WAAM-strengthened I-sections

Jiachi Yang, Pinelopi Kyvelou, M. Ahmer Wadee *, Leroy Gardner

Department of Civil and Environmental Engineering, Imperial College London, London, SW7 2AZ, UK

ARTICLE INFO

Keywords:
Finite element analysis
Numerical simulation
Prestressed member
Residual stress distribution
Wire arc additive manufacturing
WAAM-strengthened I-sections
3D printing

ABSTRACT

The use of wire arc additive manufacturing (WAAM) as a means of strengthening conventional steelwork is an emerging area of research. An experimental study has revealed that the residual stress distribution in WAAM-strengthened (at the flange tips) I-sections differs significantly from that of a typical hot-rolled I-section, owing to the thermal prestressing arising during WAAM; thus, the establishment of a bespoke residual stress model for WAAM-strengthened I-sections is required. In this paper, 3D thermal–mechanical finite element (FE) modelling is employed to predict the residual stress distributions in WAAM-strengthened I-sections, using two modelling methods — a 3D-transient method and a simplified semi-static method; both modelling methods are shown to provide an accurate representation of experimental observations, with the latter being more computational efficient. Further improvements in computational efficiency, with almost no compromise in accuracy, are achieved through the introduction of a hybrid numerical–analytical approach. The proposed approach uses the simplified semi-static method to simulate the first WAAM layer only and an analytical modification to allow for multi-layer WAAM stiffeners. Using the hybrid approach, a parametric study is performed in which numerical simulations on a total of 524 benchmark members with varying geometric properties covering a wide range of UK and European I-sections are carried out. Based on the obtained results, predictive expressions for the residual stress distributions in WAAM-strengthened I-sections are developed; the predicted residual stress patterns are shown to be in good agreement with both experimental and numerical results. Use of these expressions is recommended to determine the pattern and magnitude of residual stresses in WAAM-strengthened I-sections for the purposes of numerical simulations and the development of structural design provisions.

1. Introduction

In recent years, metal additive manufacturing (AM), also known as 3D printing, has gained increasing attention within several engineering disciplines, owing to its capability of achieving complex bespoke geometries, increased automation, as well as material and cost savings [1,2]. Wire arc additive manufacturing (WAAM) is a directed energy deposition (DED) method of metal AM, which utilises automated metal inert gas (MIG) welding for depositing the feedstock material in a layer-by-layer fashion. Being able to achieve high deposition rates (i.e., about 1 kg/h for titanium and 3 kg/h for steel [3]) and, thus, rapidly produce large-scale elements, WAAM is deemed to be the most suitable metal 3D printing method for the construction industry [4–11]. One of the most promising potential uses of WAAM within the construction sector is for the strengthening, retrofitting and repair of steel structures [1], which may be necessitated due to deterioration of structural steel during its service life, exposure to accidental actions (e.g., explosions, impacts and earthquakes) or repurposing of structural elements, to cover larger load carrying capacity demands. Structural strengthening is usually implemented by the addition of steel cover plates [12,13] or fibre reinforced polymer (FRP) plates [14], to structural members. More recently, the use of shape memory alloys (SMA) has also been explored for preventing or delaying the fatigue failure of steel structures, by harnessing the recovering nature of SMAs under thermal cycles to introduce compressive stress in cracked regions [15,16]. The addition of cable stays offers another strengthening option [17]. WAAM is envisaged to be an attractive alternative to current structural strengthening methods, as it allows the targeted deposition of the optimum amount of material at key locations, while being more accommodating of curved or uneven surfaces, on which the addition of FRP or steel cover plates may be impractical [1]. As well as strengthening existing structures, WAAM can also be used in conjunction with conventional structural steel to form efficient hybrid members for new construction [1,4]. In a pioneering study on hot-rolled I-section columns strengthened by

* Corresponding author.
E-mail address: a.wadee@imperial.ac.uk (M.A. Wadee).

https://doi.org/10.1016/j.istruc.2024.107248
Received 28 May 2024; Received in revised form 14 August 2024; Accepted 3 September 2024
Available online 17 September 2024

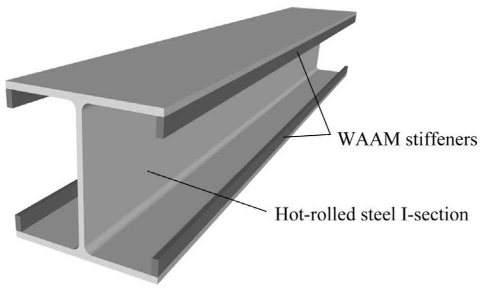

Fig. 1. Schematic illustration of WAAM-strengthened I-section member.

WAAM stiffeners at the flange tips (see Fig. 1), conducted by Gardner et al. [18], increases in axial capacity of between 17% and 54% were achieved for increases in mass of between just 2% and 26%.

As is also the case for traditional arc welding, the high heat input during WAAM can induce high residual stresses and distortion in welded/printed parts [19]. These residual stresses can be measured experimentally and predicted using numerical methods. Rossini et al. [20] reviewed the key experimental residual stress measurement methods, including semi-destructive methods, such as centre-hole drilling and deep-hole drilling, as well as non-destructive methods, such as X-ray diffraction and neutron diffraction. One of the most commonly employed techniques for residual stress measurements in structural elements is the destructive 'sectioning' method [21–23], where the residual stresses are evaluated based on the elastic strains released upon the extraction of a series of strips. Using the sectioning method, Kyvelou et al. [24] undertook residual stress measurements on three hot-rolled I-sections strengthened by the addition of WAAM stiffeners at the flange tips. It was shown that the heat input induced during WAAM effectively reversed the original underlying residual stress pattern in hot-rolled sections, which features compressive stresses at the flange tips, with one having high tensile stresses at the flange tips. The subsequent column buckling tests presented in [18] revealed that the new residual stress pattern had a beneficial impact on axial load-bearing capacity.

Following advances in computational mechanics, finite element modelling now offers a viable means of predicting residual stresses in structural members [25], as well as simulating their influence on structural members under load [26,27]. The former capability is exploited in the present research to model numerically the residual stress distribution in WAAM-strengthened I-sections [18,24]. Firstly, the existing physical experiments used for the validation of the developed FE models are summarised. The adopted FE modelling approaches are then described. Following model validation, a hybrid numerical–analytical approach for the determination of the residual stress distributions in WAAM-strengthened I-section members is presented, which uses the simplified semi-static method to simulate the first WAAM layer only and an additional modification to allow for multi-layer WAAM stiffeners using a proposed equivalent prestressed tendon method. This hybrid approach further improves the computational efficiency with almost no compromise in accuracy. The strengthened I-section members with only a single WAAM layer, as simulated numerically in the hybrid approach, are referred to as benchmark members throughout this paper. A comprehensive parametric study, in which numerical simulations on a number of benchmark members with a range of cross-sections and WAAM-stiffener geometries, are carried out subsequently. Based on the obtained numerical results, predictive expressions are given for the residual stress distributions in the simulated benchmark members, namely the benchmark distributions, through ordinary least squares regression analyses. A predictive model to describe the residual stress pattern in WAAM-strengthened I-sections, allowing for multi-layer WAAM stiffeners, is established by modifying the benchmark distributions using the equivalent prestressed tendon method. The predictive model is found to provide an accurate representation of both experimental observations and numerical simulations.

Table 1
Process parameters used for WAAM stiffeners.

Process parameters	Value
Wire grade	ER70S-6
Wire diameter (mm)	1.2
Voltage (V)	17
Current (A)	200
Travel speed (mm/s)	11
Wire feed rate (m/min)	6

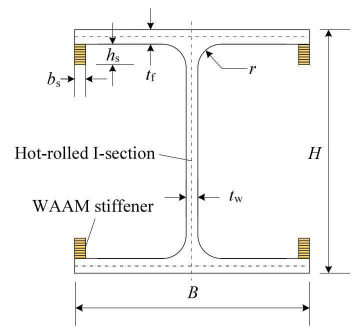

Fig. 2. Geometric properties of WAAM-strengthened I-sections.

2. Existing residual stresses measurements

A summary of the experimental programme carried out by Kyvelou et al. [24], which serves as the basis for the validation of the numerical models established herein, is presented in this section.

2.1. Examined specimens

In [24], Kyvelou et al. measured the residual stress distributions in three WAAM-strengthened I-sections using the sectioning method; one bare I-section was also measured for reference. The strengthened specimens comprised hot-rolled UC 152 × 152 × 23 profiles in Grade S355 steel and WAAM stiffeners printed from ER70S-6 unalloyed welding wire with a diameter of 1.2 mm. The process parameters employed during printing of the WAAM stiffeners are presented in Table 1. The adopted labelling system of the strengthened specimens starts with the letter S, followed by the nominal height of the WAAM stiffeners in mm, while the bare specimen is denoted as B. Note that two of the strengthened specimens had a nominal stiffener height equal to 24 mm, and were thus labelled S-24a and S-24b. The geometric properties of the WAAM-strengthened I-sections, which are schematically illustrated in Fig. 2 and listed in Table 2, were measured by means of 3D laser scanning. Note that the average height and width of each weld layer was approximately 6.5 mm and 1.4 mm respectively. The measured geometries of the specimens were adopted in the FE models introduced in Section 3.

Four stiffeners were printed on each strengthened specimen, following the building sequence illustrated in Fig. 3(a). The direction of material deposition was the same for all layers. Note that the specimens were inverted and repositioned on the worktable after the manufacture of stiffeners St_1 and St_2, as shown in Fig. 3(b), for the robotic welding arm to print the remaining two stiffeners.

2.2. Determination of mechanical properties

The material properties of the base hot-rolled I-sections and the WAAM stiffeners were determined by means of tensile coupon testing, carried out at room temperature, in the same manner as described in [28,29], in accordance with EN ISO 6892-1 [30]. A detailed description of the conducted tests and of the obtained results can be found in [24]. The average material properties determined from the

Table 2
Geometric properties of specimens measured by 3D laser scanning.

Specimen-ID	Number of weld layers in each stiffener	H	B	t_f	t_w	r	h_s	b_s
()	()	(mm)	(mm)	(mm)	(mm)	(mm)	(mm)	(mm)
B	–	152.54	151.97	6.45	6.01	12.18	–	–
S-8	6	151.90	152.45	6.75	6.06	10.36	8.18	6.59
S-24a	18	152.24	152.20	6.73	6.04	10.14	24.13	6.71
S-24b	18	152.19	151.59	6.77	6.04	10.18	24.29	6.35

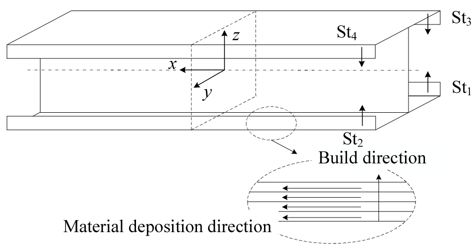

(a)

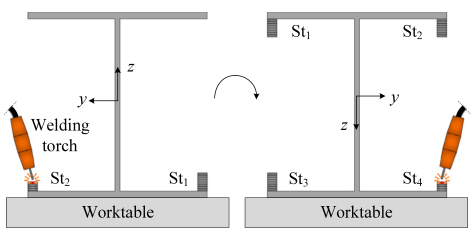

(b)

Fig. 3. (a) Building sequence of WAAM stiffeners and direction of material deposition and (b) inversion of specimens during WAAM of stiffeners St_3 and St_4.

Table 3
Average mechanical properties obtained from tensile coupon tests [24].

Steel type	Coupon location	E (MPa)	f_y (MPa)	f_u (MPa)	ε_u	ε_f
Hot-rolled	I-section	210 500	413	565	0.145	0.370
WAAM	WAAM stiffener	212 600	406	526	0.126	0.313

aforementioned tests are presented in Table 3, where E, f_y, f_u, and ε_u, ε_f are the Young's modulus, the yield strength, the ultimate tensile strength, the strain at f_u and the fracture strain measured in compliance with EN ISO 6892-1 [30] respectively. Note that the tensile coupons extracted from the WAAM stiffeners were loaded parallel to the print layer orientation.

2.3. Measured residual stresses

In [24], it was found that the original underlying residual stress pattern of the studied hot-rolled I-sections was effectively reversed after the addition of the WAAM stiffeners at the flange tips, due to the thermal prestressing effect of WAAM. High tensile residual stresses, almost equal to the yield stress of the material — f_y, were observed at the flange tips (replacing the underlying compressive stresses at these locations), while the magnitude of the compressive residual stresses in the web increased to achieve self-equilibrium across the cross-section. Since the reversal of the residual stress pattern is primarily attributed to the localised heat input to the flange tips during the WAAM process, it is largely independent of the amount of WAAM material deposited. The residual stress measurements introduced above are used in the subsequent sections of this paper for the validation of the developed FE models and the assessment of the proposed predictive expressions.

3. Finite element analysis

3.1. Introduction

The numerical simulation of the residual stresses arising within steel elements during welding is commonly undertaken using a 3D transient thermal–mechanical FE modelling method, termed herein as the 'transient' method [31–35]. The accuracy of this method, which replicates the full welding process, is high, but the analyses are computationally expensive. While some benchmark analyses have been performed herein using the transient method, most analyses have been carried out using a more computationally efficient FE simulation method termed the 'semi-static' method, which features a layer by layer heating approach, as described in [36,37]. Both methods involve a two-stage sequential thermal–mechanical analysis, with the thermal and the mechanical components assumed to be decoupled [38]. In this section, the material properties adopted in the FE models are first introduced, followed by the descriptions of the employed FE modelling methods — the transient and the semi-static method respectively, including the key features of the thermal and the mechanical analyses for both methods. The model validation is presented thereafter. All numerical simulations were carried out using the commercial FE package ABAQUS [39].

3.2. Thermal and mechanical properties

The thermal properties for carbon steel at elevated temperatures, as provided in EN 1993-1-2 [40], were employed in the present study, including the temperature-dependent thermal conductivity λ, specific heat c, and thermal elongation $\Delta L/L$. Note that the models for λ and c used in the conducted numerical simulations were adjusted to suit the examined welding scenarios and to avoid computational singularities. More specifically, as suggested by Ding [41], λ was artificially increased for temperatures exceeding the melting point of steel (i.e., approximately 1500 °C) in order to account for the convective heat transfer within the weld pool. Furthermore, the spike in the EN 1993-1-2 specific heat model at around 730 °C, corresponding to the phase transformation of steel from ferrite (α-Fe) to austenite (γ-Fe), was artificially lowered to avoid computational singularities; this approach has been shown in [42] to have little influence on the computational accuracy of welding simulations. The models adopted for λ and c are shown in Fig. 4(a), while the model for thermal elongation, as given in EN 1993-1-2 [40], is plotted in Fig. 4(b), with the plateau between 750 °C and 850 °C corresponding to the phase transformation of steel.

The stress–strain model of carbon steel at elevated temperatures, with strain-hardening, as given in EN 1993-1-2 [40], is employed in the conducted FE analyses. The stress–strain curve, shown in Fig. 5(a), is characterised by the Young's modulus E_θ, the proportionality limit $f_{p,\theta}$, the effective yield strength $f_{y,\theta}$ (corresponding to the stress at 2% total strain), and the ultimate strength $f_{u,\theta}$, given by Eq. (1). Note that the subscript θ denotes elevated temperatures.

$$f_{u,\theta} = \begin{cases} 1.25\, f_{y,\theta} & (\theta < 300\ ^\circ\text{C}) \\ f_{y,\theta}\,(2 - 0.0025\,\theta) & (300\ ^\circ\text{C} \le \theta < 400\ ^\circ\text{C}) \\ f_{y,\theta} & (\theta \ge 400\ ^\circ\text{C}) \end{cases} \tag{1}$$

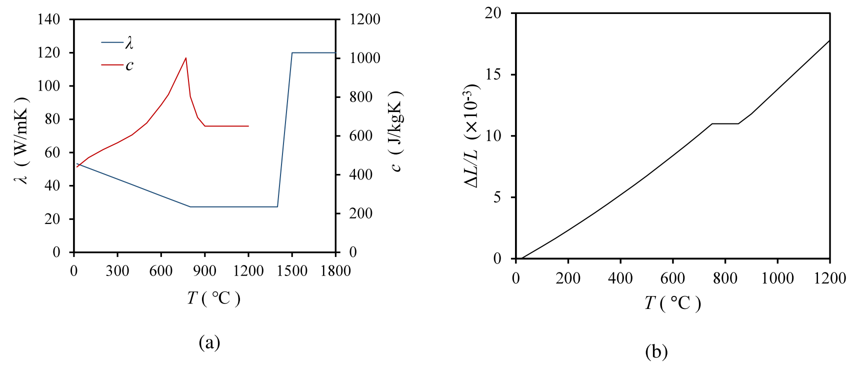

Fig. 4. (a) Adjusted thermal conductivity λ and specific heat c and (b) thermal elongation $\Delta L/L$ against temperature T.

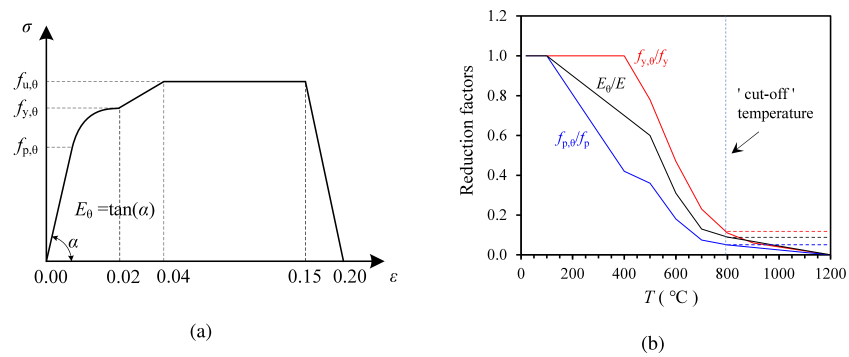

Fig. 5. (a) Stress–strain relationship with strain-hardening at elevated temperatures and (b) reduction factors for E_θ, $f_{p,\theta}$ and $f_{y,\theta}$ [40].

The values of E_θ, $f_{p,\theta}$ and $f_{y,\theta}$ can be obtained by multiplying their values at room temperature (i.e., E, f_p, and f_y respectively) with the reduction factors plotted with the solid lines in Fig. 5(b) [40]. As recommended in [43], to avoid computational non-convergence, a 'cut-off' temperature of 800 °C was employed, beyond which the material strengths and Young's modulus remain unchanged — see Fig. 5(b). Finally, a constant Poisson's ratio of 0.3 and a density of 7850 kg/m^3 were adopted.

3.3. FE simulations

In [44], Shanghvi et al. showed that for an infinitely long weld line, the welding temperature field reaches a steady state when observed in an Eulerian frame travelling along with the welding heat source, known as the 'long weld' assumption; this results in a uniform residual stress field along the longitudinal direction of the welded element. In reality, despite some end-effects, the 'long weld' assumption is deemed valid for a finite-long welded member, provided that its length is sufficient for the development of a uniform residual stress region. According to [21], in prismatic steel members, residual stresses are fully developed at a distance of 1.5 to 2.0 times the transverse dimension of the cross-section (i.e., B) to the end of the member; thus, on the merit of this principle, the 2000 mm long specimens tested in [24] and modelled herein were represented by 600 mm long cuts in the FE models for computational efficiency, corresponding to a length to height ratio of approximately 4 (see Fig. 6).

The thermal and mechanical FE models were meshed using the linear heat transfer hexahedron elements DC3D8R with reduced integration and the 8-node linear brick element C3D8R with reduced integration and hourglass control respectively [39]. The mesh of a typical specimen is shown in Fig. 7(a). Each weld line had four elements across its width and one element over its height. For the base I-section, the element size was increased with increasing distance from the stiffener (weld) regions along the three arrow directions ('A', 'B' and 'C', in Fig. 7(b)) with a ratio of 1.2 being adjacent rows of elements. In the longitudinal direction, a constant mesh size of 5 mm was used. Note that the selection of the employed mesh sizes was made following a mesh sensitivity study.

Table 4
Characteristic parameters of the hemispherical moving heat source.

Q (W)	γ	r (mm)	v_t (mm/s)
3400	0.9	3.25	11

3.3.1. Thermal analysis

3.3.1.1. Transient method. In the transient method, the welding heat source was simulated in the DFLUX subroutine [39] using a moving hemisphere power density model [45], as shown in Fig. 8(a), where x, y and z are the coordinates of a Lagrangian frame that is fixed in space and ξ is a Eulerian coordinate that travels with the heat source. The power density q (W/m^3), which can be determined using Eqs. (2) and (3), follows Gaussian distributions in the two in-plane directions, as shown in Fig. 8(b).

$$q(\xi, y, z) = \frac{6\sqrt{3}\gamma Q}{r^3\pi^{3/2}} e^{-3(\xi^2+y^2+z^2)/r^2} \tag{2}$$

$$\xi = x - v_t t \tag{3}$$

In Eqs. (2) and (3), Q is the gross welding power calculated as the product of the average voltage V and current I from Table 1, γ is the thermal efficiency, r is the radius of the hemisphere taken as half the width of the weld layer and v_t is the travel speed of the welding torch. The values of these parameters, as used in the experimental study [18,24] and assumed in the thermal analysis, are listed in Table 4.

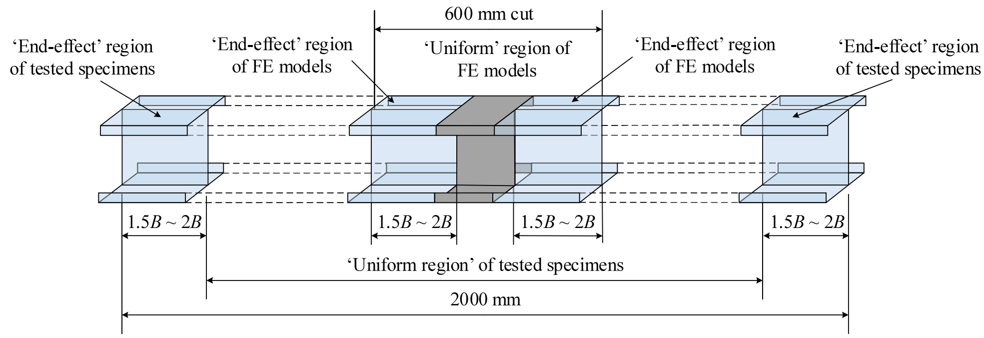

Fig. 6. Schematic illustration of the uniform region and end-effect regions of the tested and modelled specimens.

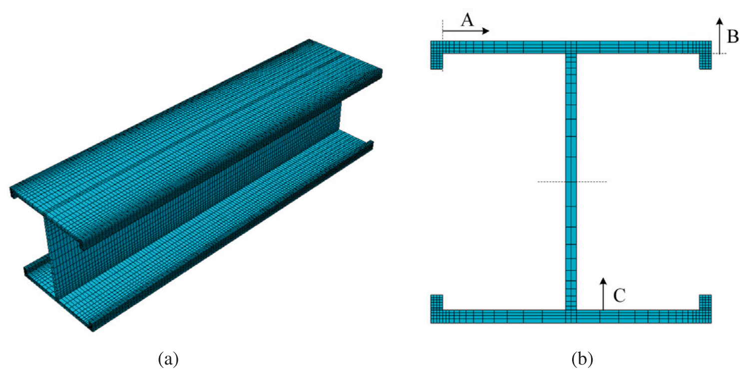

Fig. 7. FE mesh of a typical specimen (Specimen S-8-T): (a) overall view and (b) cross-section.

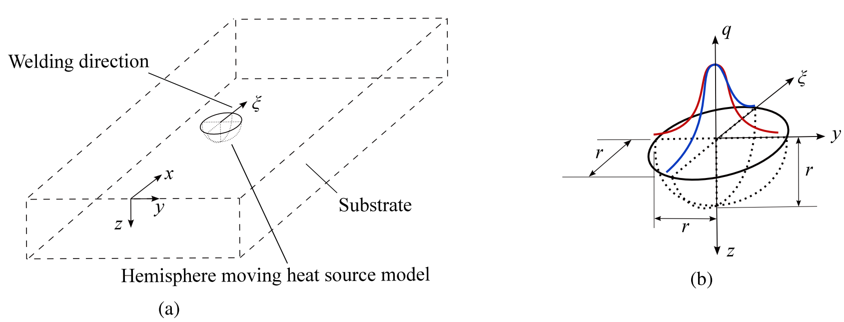

Fig. 8. Moving power density model: (a) schematic illustration and (b) Gaussian distributions.

The *MODEL CHANGE command [39], which allows the addition and removal of a model region during an FE analysis, was used to replicate the material deposition. All weld lines were deactivated (i.e., removed) in the first step of the analysis, and then added progressively in a layer-by-layer fashion, following the building sequence. An inter-layer dwell time of 1000 s was employed for the whole model before the activation of a new weld layer. This inter-layer dwell time corresponds to that employed in the recent production of WAAM-strengthened beam specimens; shorter times could be employed in practice but the effect on the resulting residual stress pattern is expected to be minimal. Two heat transfer coefficients – the film coefficient and emissivity – were assigned to the outer surfaces of the models to allow for the heat loss through convection and radiation; the assigned values were 20 W/(m^2 K) and 0.2 respectively, determined by calibration against the experimental results. The heat sink effect of the table was inherently allowed for in the choice of the film coefficient and emissivity required to achieve the approximate rate of cooling observed in the experiments.

3.3.1.2. Semi-static method. For the semi-static method, the welding heat input was not explicitly modelled using a moving power density model as in the transient method, but by prescribing temperature fields at the weld regions, following a 3-step procedure using a pseudo unit time — see Fig. 9, where T is the temperature and t is the time.

In the first step, the entire boundary of a weld layer is preheated up to a temperature T_p in a duration of t_p, achieved by linearly ramping up the nodal temperatures at the weld layer boundary. During the second step, the temperature T_p is kept constant along the weld layer boundary for a duration of t_h, allowing the surrounding elements to heat up. Note that T_p must be higher than the temperature corresponding to the melting point of steel, so that a fusion (or molten) zone is generated in the FE model. Finally, in the third step, the entire weld layer (i.e., not just its boundary) is activated (i.e., added) with an initial temperature equal to T_p, followed by an inter-layer dwell time of 1000 s. The values of T_p, t_p and t_h were determined via a trial-and-error procedure, in order for the penetration depth of the fusion zone of the FE model to match that of the experimental observation, which was measured

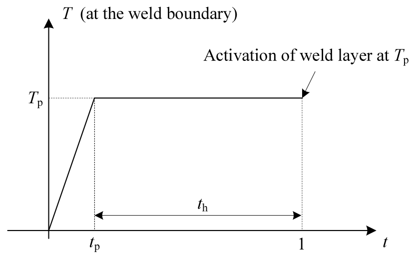

Fig. 9. Schematic illustration of the 3-step procedure used to prescribe temperature fields.

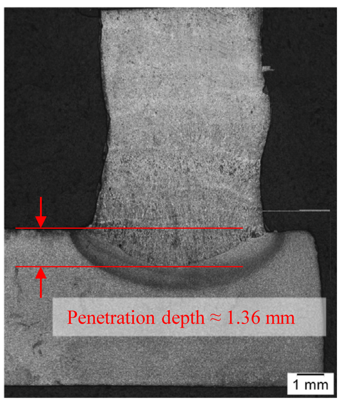

Fig. 10. Micrograph showing weld penetration depth in Specimen S-24a.

through a micrograph of the intersection between the WAAM stiffener and the base section for Specimen S-24a [24] — see Fig. 10. Note that although more than one combination of T_p, t_p and t_h satisfy the aforementioned condition, a sensitivity study carried out by the authors showed that the influence of the different combinations on the resulting numerical residual stress distributions is negligible. Thus, the adopted values of T_p, t_p and t_h were 1800 °C, 0.1 s and 0.9 s respectively. The described 3-step procedure was repeated for all weld layers, following the building sequence. The adopted values of the film coefficient and emissivity were the same as those used in the transient method.

Finally, it should be mentioned that the transient variation of the temperature fields arising from the movement of the welding heat source between the onset and the end of the deposition of each weld layer, are not modelled in the semi-static method, since each weld layer is heated by a uniform temperature field prescribed along its entire length in a pseudo unit time. Though the movement of the welding heat source is neglected, the building sequences of the WAAM layers are still considered; this feature is indicated by the name of this method.

3.3.2. Mechanical analysis

For both the transient and the semi-static method, the element removal/addition sequences in the thermal models are maintained in the subsequent mechanical analyses. The temperature fields for all increments of the thermal analysis were sequentially imported into the mechanical model as thermal loads, using the *PREDEFINED FIELDS command [39]. Finally, the resulting residual stress fields can be determined based on the thermal expansion and contraction arising from the imported thermal loads.

The adopted boundary conditions during the mechanical analysis were applied to replicate the clamping and inversion of the specimens on the worktable during manufacturing of the stiffeners (see Fig. 3(b)), achieved by restraining the outer surface of the bottom and top flange along the z-direction in turn — see Fig. 11. Note that these restraints were released for the final step of the analysis. Additionally, as shown in Fig. 11, boundary conditions that prevent rigid body motion were applied at the centroids of the two end sections throughout the analysis.

Table 5
Summary of CPU times of the conducted FE simulations (unit: s).

Model ID	Thermal analysis	Mechanical analysis	Total
S-8-T	198 964	120 535	319 499
S-8-S	2898	5310	8208
S-24a-S	10 921	19 890	30 811
S-24b-S	10 915	19 901	30 816

Another key aspect of the mechanical simulation is the original underlying residual stress distribution in the base hot-rolled I-sections. A number of residual stress models have been proposed and adopted for hot-rolled I-sections [46–49]; some typical examples are shown in Fig. 12, with the residual stresses through the thickness of the section assumed to be uniform.

The original underlying residual stress distribution in the bare I-section specimen (Specimen B) was measured in [24] and is shown in Fig. 13, where $\bar{y}$ and $\bar{z}$ are equal to $y/(B/2)$ and $z/(D/2)$, see Fig. 2 where $D = H - t_f$, and $\bar{\sigma}$ is the ratio of the measured residual stress to the yield stress f_y. Note that tensile stresses are observed at the tips of the lower flange of Specimen B from the experimental measurements, which contradicts the typical residual stress pattern of hot-rolled I-sections (see Fig. 12). This is likely attributed to straightening of the member during production [24]. For the model validation performed herein, a multi-linear initial residual stress distribution, following the shape of the ECCS residual stress model (see Fig. 12(c)), but with the magnitudes from the experimental measurements of Specimen B, as shown in Fig. 13, was applied to the bare I-sections.

3.4. Validation against experimental data

The residual stress distribution in Specimen S-8 measured in [24] was simulated herein using both the transient and the semi-static method, with the results of the former providing a reference for those of the latter. The remaining two specimens were simulated using the semi-static method only. The modelled specimens are labelled following the same convention as the respective test specimens in [24] (see Section 2.1), with the extra letter 'T' or 'S' at the end, indicating which FE simulation method was employed (i.e., 'T' for transient and 'S' for semi-static).

The numerical residual stress distributions at the mid-length of the three strengthened specimens are compared against the corresponding experimental measurements [24] in Fig. 14, where very good agreement can be seen. Note that for most locations of the flanges, the plotted numerical residual stresses were extracted from the outer element surfaces, for consistency with the respective experimental measurements [24]. The CPU times of the conducted FE simulations are summarised in Table 5, where it can be observed that the computational time required for the semi-static model S-8-S was only about 2% of the time required for its transient counterpart, with no significant loss in accuracy. As expected, it can be also seen that the computational time is strongly dictated by the number of the weld layers.

Comparisons between the residual stress distributions in the WAAM-strengthened specimens plotted in Fig. 14 and the original underlying residual stress patterns of the base I-sections given in Figs. 12 and 13 show that the residual stresses at the flange tips are effectively reversed from compressive to tensile due to the addition of the WAAM stiffeners. This is caused by the high thermal energy input imposed locally at the flange tips during the WAAM process, leading to local material plasticity and thermal deformations. The localised thermal contraction of the WAAM material after cooling, which is constrained by the adjacent material, leads to the generation of high tensile residual stresses at the flange tips. Overall, high tensile residual stresses, with a relatively uniform distribution, can be observed across the height of

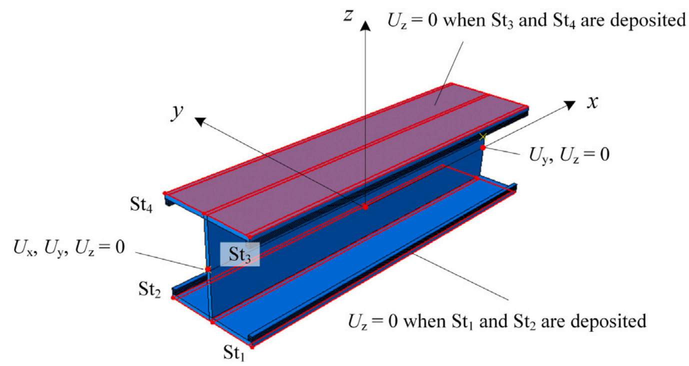

Fig. 11. Boundary conditions in mechanical simulations (U_x, U_y, U_z — translations in the x, y and z directions respectively).

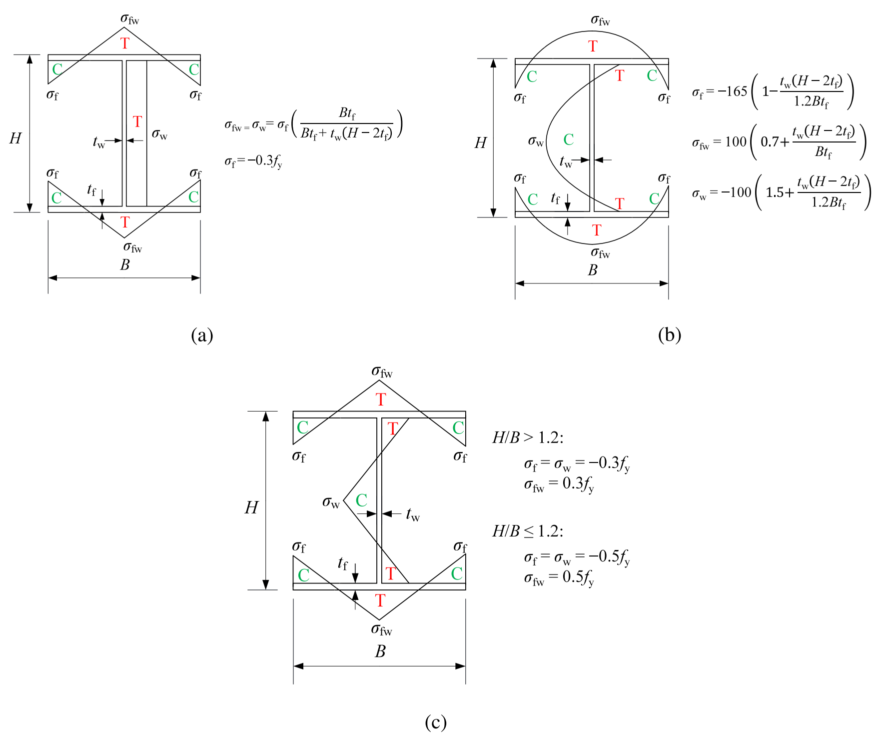

Fig. 12. Residual stress models: (a) for US wide flange beams [46], (b) parabolic [48] and (c) ECCS model for hot-rolled I-sections [47] (T = tension, C = compression).

WAAM stiffeners. As expected, the cross-section regions away from the flange tips, such as at the web and the web-to-flange junctions, are less affected by the welding heat input, and, thus, the shape of their initial residual stress pattern is largely preserved. Note that the magnitudes of the compressive residual stresses in the web increase relative to the web of the unstrengthened section to maintain cross-section force equilibrium. It should be mentioned that, even though the geometries of Specimens S-24a and S-24b were nominally the same, their residual stress distributions at the bottom flange were approximately reflected about the vertical axis — see Fig. 14(b) and (c). This is attributed to the different building sequence of the WAAM stiffeners of these two specimens (St_1 – St_2 – St_3 – St_4 for Specimen S-24a, and St_2 – St_1 – St_3 – St_4 for Specimen S-24b), confirmed by the manufacturer, which indicates that the order in which the stiffeners are printed has an influence, albeit minor, on the final pattern of the residual stresses. The average residual stresses in the WAAM stiffeners of the three specimens, normalised by the yield stress f_y of the WAAM material, are shown in Table 6. It can be observed that the magnitude of the average residual stress decreases with an increasing number of weld layers, due to the changing proportions of the I-section relative to the stiffeners, and hence the changing level of restraint. This phenomenon is analysed and harnessed in the equivalent prestressed tendon method employed in the next section, and forms the foundation of the subsequent parametric study.

Table 6
Normalised average residual stresses in the WAAM stiffeners of the examined specimens.

Model ID	Number of weld layers of each WAAM stiffener	Normalised average residual stress σ/f_y
S-8-S	6	0.98
S-24a-S	18	0.85
S-24b-S	18	0.85

The 3D residual stress and deformation fields of the FE model S-8-S are presented in Fig. 15(a), while the cross-sectional residual stresses and distortion at the end and mid-length of the modelled specimen are shown in Fig. 15(b) and (c) respectively. The cross-sectional distortion

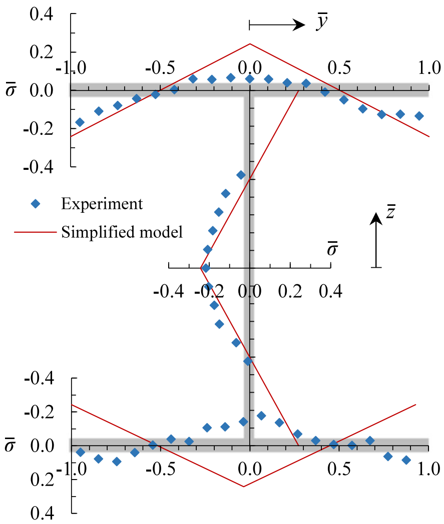

Fig. 13. Measured residual stress distribution in Specimen B [24], and adopted simplified residual stress distribution for the FE model validation.

arises from the eccentric thermal contraction of the WAAM stiffeners relative to the local centroid of the flange tip. Furthermore, the distorted cross-section profiles at the end and mid-length of the FE models S-8-S, S-24a-S and S-24b-S are plotted in Fig. 16, where δ_y and δ_z are the deformations in the y and z directions, respectively.

4. Hybrid numerical–analytical predicting approach

Although the semi-static method introduced in Section 3 has been shown to be efficient and accurate, extensive computational efforts are still required for its implementation, especially for strengthened I-sections with multi-layer WAAM stiffeners. This presents significant challenges for a comprehensive FE parametric study aiming to explore residual stresses in WAAM-strengthened I-section members with a wide range of geometries. A hybrid numerical–analytical approach is therefore proposed, in which a thermal–mechanical FE simulation is performed for the first layer of the WAAM stiffeners, and modifications to the simulated results are made to allow for the subsequent layers using a proposed equivalent prestressed tendon method.

4.1. Equivalent prestressed tendon method

For a generic WAAM strengthened I-section member with n ($n \geq 1$) weld layers for each WAAM stiffener, a corresponding benchmark member with a single weld layer is first defined (see Fig. 17). Assuming that the residual stress distributions in the four WAAM stiffeners are identical and uniform across their height, the additional $(n-1)$ weld layers (containing $4(n-1)$ weld lines in total) can be considered as equivalent to a prestressed tendon attached to the benchmark member, as illustrated in Fig. 17. Therefore, the residual stress distribution in a generic WAAM strengthened I-section member can be regarded as the superposition of the residual stress distribution in the corresponding benchmark member and the stresses imposed by the equivalent prestressed tendon.

Once the residual stress distribution in the corresponding benchmark member has been obtained through FE analysis, the additional stresses imposed on the benchmark member by the equivalent prestressed tendon are calculated as described below. The benchmark member is initially assumed to be in a stress-free state prior to the attachment of the tendon, while the tendon is pre-tensioned with a tendon stress σ_p, as shown in Fig. 18(a). The length of the member is denoted as L. The cross-sectional areas of the base I-section and of a single weld line are designated as A_b and A_{wl} respectively. The tendon stress σ_p is determined based on the 'welding tendon force' proposed by White [50] and adopted in [51,52], according to which the magnitude of the tendon stress is related to the maximum temperature experienced by the material during welding. Note that, in line with [50,51], it is assumed that the material properties are temperature independent and that the stress–strain relationship is elastic-perfectly plastic. With these assumptions made, the 'second yield temperature' — T_{y2} [51], given by Eq. (4), is introduced and defined as the threshold temperature beyond which the tendon stress can be taken as equal to the material yield stress, f_y.

$$T_{y2} = T_0 + \frac{2\varepsilon_y}{\alpha} \tag{4}$$

In Eq. (4), T_0 is the ambient temperature, ε_y is the yield strain at T_0 (with $\varepsilon_y = f_y/E$), and α is the linear coefficient of thermal expansion taken as the first derivative of the thermal elongation with respect to temperature at T_0. Taking $T_0 = 20$ °C, $\alpha = 1.216 \times 10^{-5}$ [40], and with f_y and E of the WAAM steel obtained from Table 3, $T_{y2} = 334$ °C for the sections studied herein. Since the material in the stiffeners undergoes melting and solidification during the WAAM deposition, the peak temperature experienced exceeds the melting point of steel, which is significantly higher than T_{y2}. Hence, the tendon stress σ_p within the WAAM stiffeners is equal to $f_{y,w}$, with the subscript 'w' referring to the WAAM steel.

Having determined that the tendon stress $\sigma_p = f_{y,w}$, the final stress distribution in the equivalent prestressed member can be derived using the method introduced by Hadjipantelis et al. in [53]. Following attachment of the equivalent prestressed tendon at the cross-section centroid, the member is compressed, resulting in an end shortening δ, as shown in Fig. 18(b). The prestressed tendon is also shortened by δ, owing to deformation compatibility, leading to a reduction in the tendon stress from σ_p to σ_t:

$$\sigma_t = \sigma_p - E_w \frac{\delta}{L}, \tag{5}$$

where E_w is the Young's modulus of the WAAM stiffener material. As such, the member can be assumed to be uniformly compressed with an axial strain of ε_c (with compression being negative). To determine of ε_c, a cut is made at Section A-A, as illustrated in Fig. 18(c), where equilibrium of the compressive and tensile cross-sectional forces, F_c and F_t respectively, dictates that:

$$F_c + F_t = 0, \tag{6}$$

and hence

$$\sigma_t A_{ten} + \sigma_{c,b} A_b + 4\sigma_{c,w} A_{wl} = 0. \tag{7}$$

Here, A_{ten} is the area of the equivalent prestressed tendon:

$$A_{ten} = 4(n-1)A_{wl}, \tag{8}$$

while $\sigma_{c,b}$ and $\sigma_{c,w}$ are the compressive stresses in the base I-section and the WAAM stiffeners respectively, which are calculated as:

$$\sigma_{c,b} = E_b \varepsilon_c, \tag{9}$$

and

$$\sigma_{c,w} = E_w \varepsilon_c. \tag{10}$$

Also, for compatibility:

$$\delta = -\varepsilon_c L. \tag{11}$$

Substituting Eqs. (9)–(11) into Eq. (7) gives:

$$\varepsilon_c = \frac{4(1-n)\sigma_p A_{wl}}{E_b A_b + 4nE_w A_{wl}}. \tag{12}$$

Finally, the stresses ($\sigma_{c,b}$ and $\sigma_{c,w}$) imposed on the benchmark member by the equivalent prestressed tendon may be obtained by substituting ε_c

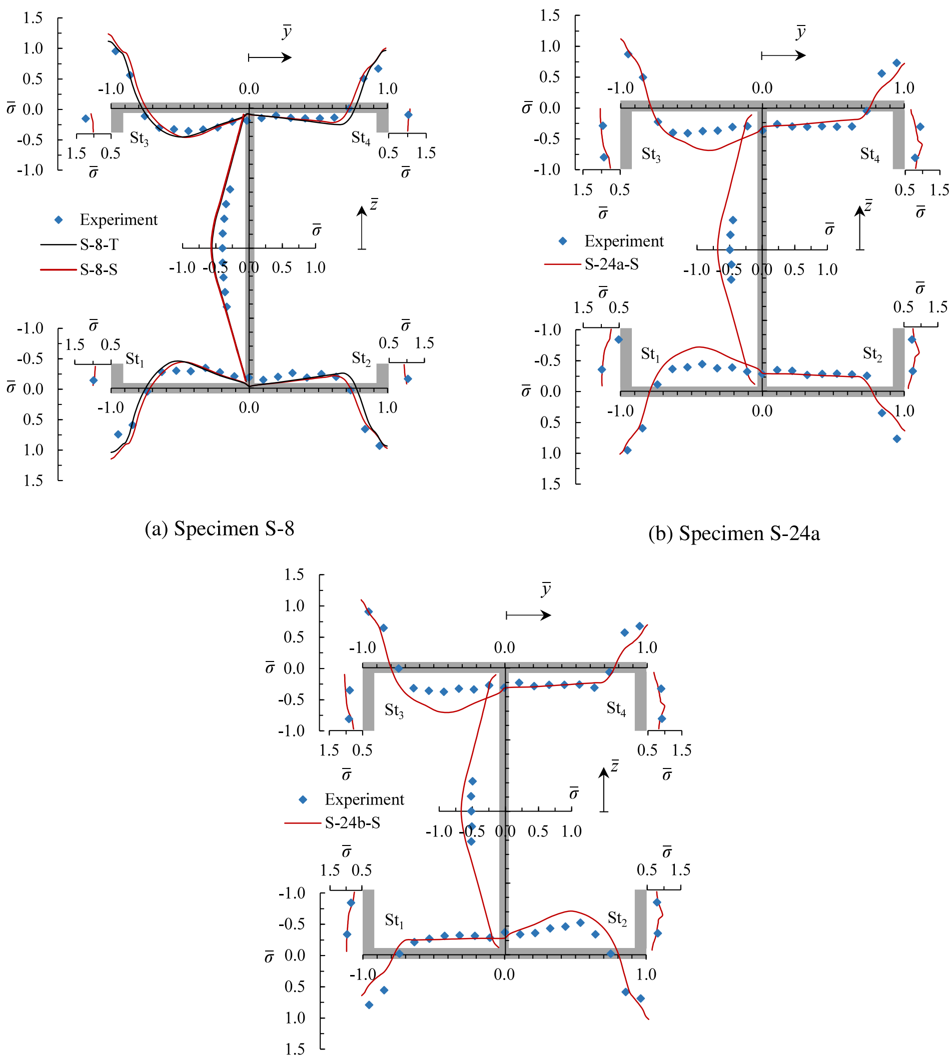

(a) Specimen S-8

(b) Specimen S-24a

(c) Specimen S-24b

Fig. 14. Numerical and experimental residual stress distributions at the mid-length of the examined WAAM-strengthened specimens.

from Eq. (12) back into Eqs. (9) and (10). Additionally, by substituting Eqs. (11) and (12) back into Eq. (5), it can be observed that the tensile stress in the tendon σ_t, corresponding to the residual stresses in the WAAM stiffeners, decreases with an increasing number of weld layers n, which is consistent with the conducted numerical simulations — see Table 6.

4.2. Validation of hybrid approach

The hybrid numerical–analytical approach was employed for the determination of the residual stress distributions in the tested WAAM-strengthened specimens; first, an FE simulation was carried out on the corresponding benchmark member using the semi-static method described in Section 3. The results were then modified using the equivalent prestressed tendon method for multi-layer WAAM stiffeners. In Fig. 19, the residual stress distributions predicted by the proposed hybrid approach for the three test specimens examined herein are plotted against the respective experimental and numerical results. Overall, the accuracy of the proposed hybrid method is very good at significantly lower computational cost compared to the full numerical model, since the simulation of only a single weld layer is required in the benchmark member. Following validation, the proposed hybrid approach is used to investigate the residual stress distribution in WAAM-strengthened I-sections with a wide range of geometric properties through the parametric study presented in the next section.

5. Parametric study

Based on the hybrid numerical–analytical approach described in Section 4, a parametric study covering a total of 524 WAAM-strengthened I-section members (single-layer benchmark members), including a wide range of UK and European hot-rolled profiles, is presented. The results are used in Section 6 to underpin the development of a predictive residual stress model for WAAM-strengthened I-sections.

The benchmark FE models (i.e., those in which a single weld layer is simulated using the semi-static method) are presented in Table 7. These models were divided into two groups according to the widths B of the underlying I-sections, where the models with widths between 100 mm and 250 mm were assigned to Group A and the models with widths between 250 mm and 350 mm were assigned to Group B. The two group of models are assigned two different weld geometries — W_A and W_B, with the latter larger in area, for the WAAM stiffeners.

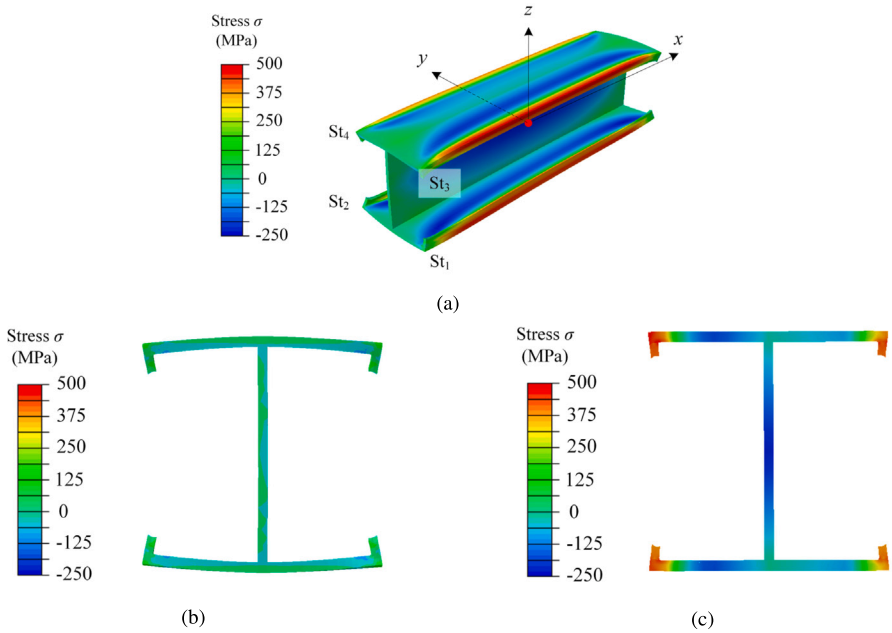

Fig. 15. Residual stress and deformation fields of FE model S-8-S: (a) full 3D profile, (b) at end cross-section and (c) at mid-length cross-section (deformation scale factor = 10).

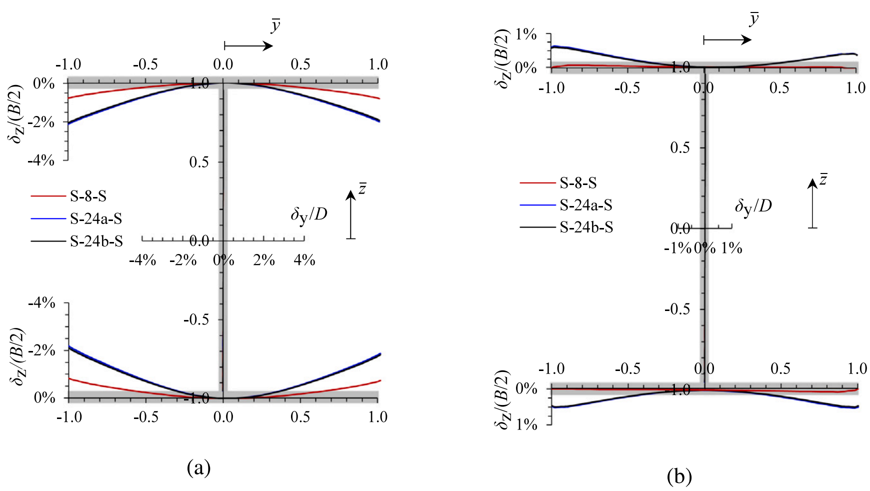

Fig. 16. Distorted cross-section profiles at (a) the end and (b) mid-length of the modelled specimens S-8-S, S-24a-S, S-24b-S (WAAM stiffeners not shown).

The employed weld geometries are deemed to be compatible with the proportions of the base sections in each group. The process parameters assumed for the manufacture of W_A and W_B are given in Tables 1 and 8 respectively.

In Fig. 20, the t_f/B and t_w/t_f ratios of a wide range of UC, UB, IPE, HEA and HEM sections are plotted against their widths B. It can be observed that most of the UK and European hot-rolled I-sections with widths less than 350 mm fall within the range of the two groups examined herein. The H/B ratio is expected to have little influence on the residual stress distribution of the strengthened specimens, since the web is largely unaffected by the welding heat input; thus the examined H/B range was not exhaustive. The length of the modelled members was four times the section height.

The benchmark models were assumed to have uniform thermal and mechanical material properties. The widely used quad-linear stress–strain curve [54–56] proposed by Yun and Gardner [57] for hot-rolled steel, as shown in Fig. 21, was employed for the constitutive stress–strain relationship of the I-sections at room temperature. The yield and ultimate tensile strengths were taken as 355 MPa and 490 MPa respectively, in accordance with EN 1993-1-1 [58]. The EN 1993-1-2 [40] material model described in Section 3 was adopted at elevated temperatures, while the ECCS residual stress distribution [47] shown in Fig. 12(c) was assigned to the modelled sections. For the models in Group A and Group B, the values of T_p, t_p, and t_h adopted in the semi-static method were taken as 1800 °C, 0.1 s and 0.9 s, and 1900 °C, 0.1 s and 0.9 s respectively. The obtained results are examined in Section 6 and used as the basis for the development of a predictive model for residual stresses in WAAM-strengthened I-sections.

6. Predictive residual stress model

A predictive residual stress model for WAAM-strengthened I-sections, characterised by five parameters, is proposed in this section. The influence of the geometric properties of the WAAM-strengthened I-sections on these five parameters is analysed, based on the results of the parametric study (see Section 5). The predictive model is subsequently developed using ordinary least squares regression, in conjunction with the equivalent prestressed tendon method (see Section 4.1).

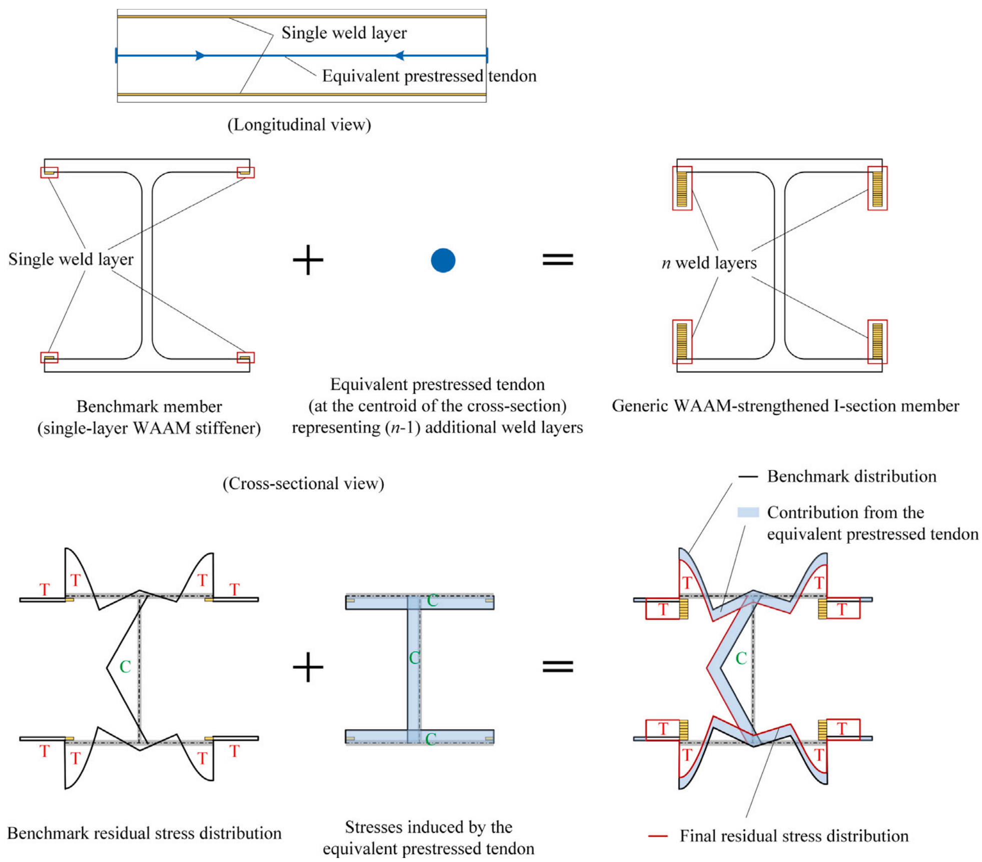

Fig. 17. Schematic illustration of a generic WAAM-strengthened I-section member, simplified into two components: a corresponding benchmark member and an equivalent prestressed tendon, and the illustration of the superposition of residual stresses (T = tension, C = compression).

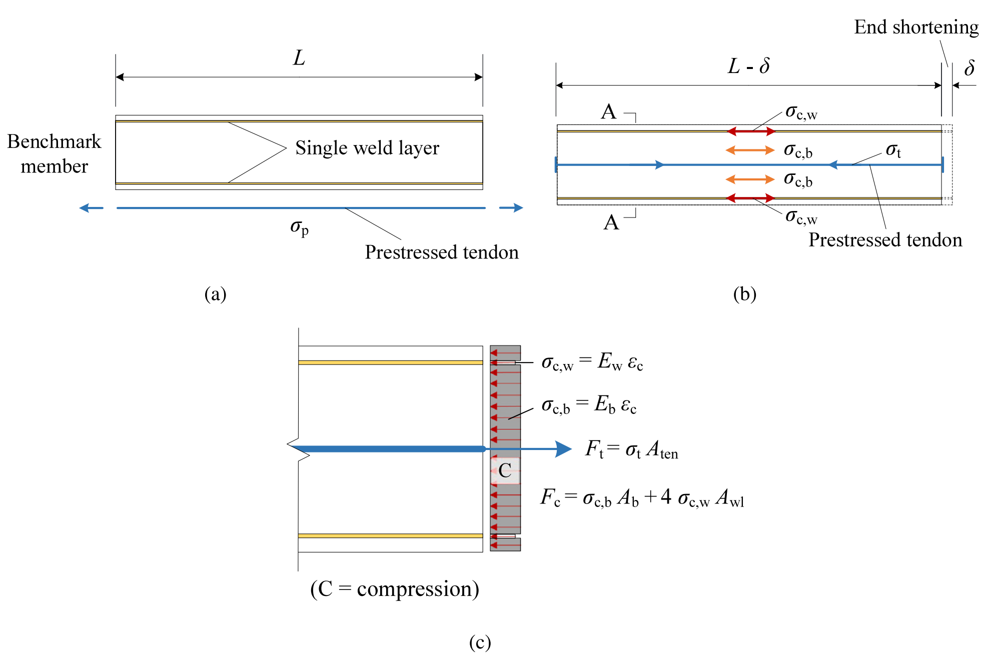

Fig. 18. Benchmark member (a) before and (b) after attachment of the equivalent prestressed tendon and (c) stress distribution on free-body cut at Section A-A.

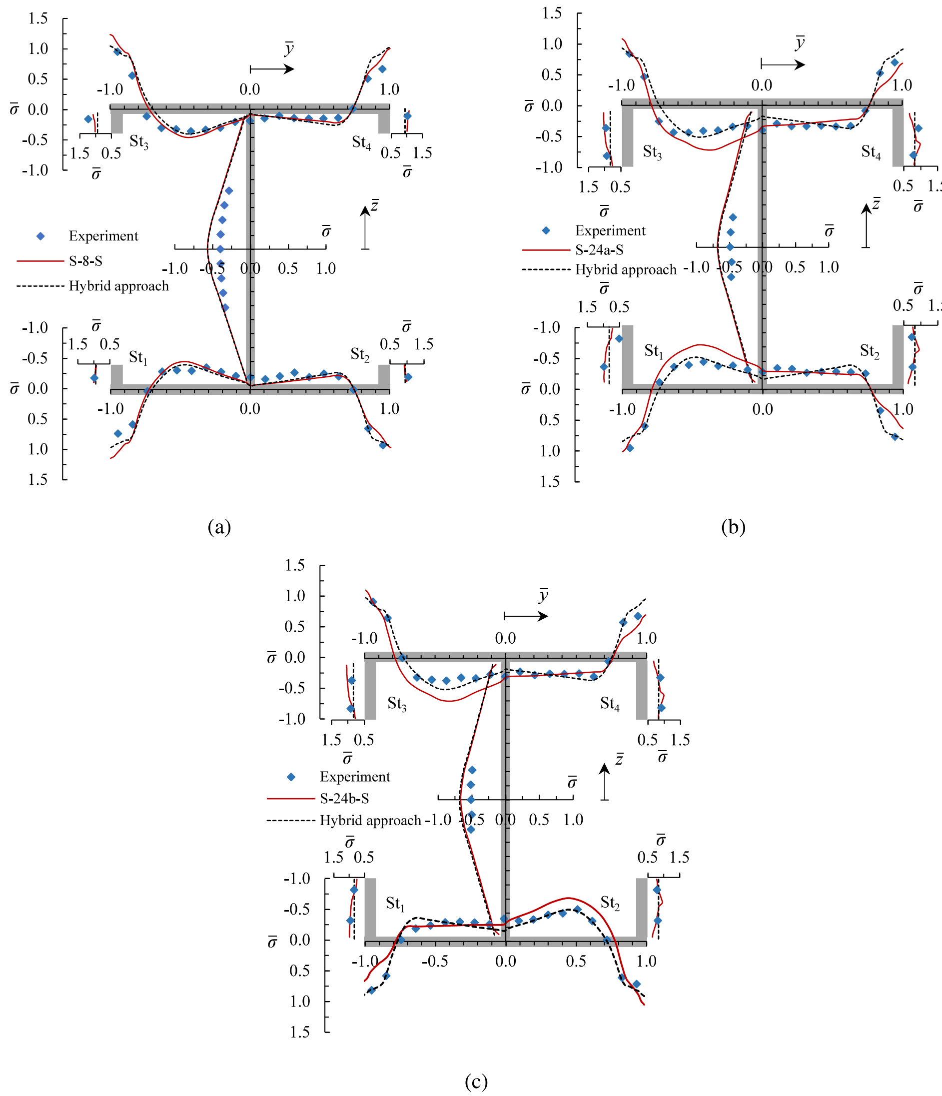

Fig. 19. Residual stress distributions of Specimens (a) S-8, (b) S-24a and (c) S-24b, as obtained using the hybrid approach, full numerical models and from the experiments [24].

Table 7
FE models of benchmark members for parametric study.

Benchmark models	Weld dimensions (Width × Height) (mm)	Modelling parameter	Examined range
Group A (100 mm ≤ B < 250 mm)	W_A : 6.5×1.4	B (mm)	100, 125, 150, 175, 200, 225
		H/B	1.0, 1.5, 2.0
		t_f/B	0.04, 0.06, 0.08, 0.10, 0.12, 0.14
		t_w/t_f	0.5, 0.6, 0.7, 0.8
Group B (250 mm ≤ B ≤ 350 mm)	W_B : 9.8×2.25	B (mm)	250, 275, 300, 350
		H/B	1.0, 1.5
		t_f/B	0.04, 0.06, 0.08, 0.10, 0.12, 0.14 for $H/B = 1.0$ 0.04, 0.06, 0.08, 0.10, 0.12, 0.14, 0.16, 0.20 for $H/B = 1.5$
		t_w/t_f	0.5, 0.8

6.1. General residual stress pattern

Although, owing to the sequential nature of the welding, some degree of asymmetry has been observed in the measured and simulated residual stress distributions (see Fig. 14), to reduce the complexity of the residual stress model, a simplified doubly-symmetric multi-linear pattern is proposed herein, as shown in Fig. 22(a). This residual stress distribution can be regarded as the superposition of the benchmark residual stress distribution and the stresses imposed by the equivalent prestressed tendon, as described in Section 4.1 and shown in Fig. 22(b). The benchmark distribution is characterised by five parameters – $\bar{\sigma}_{tip,b}$, $\bar{\sigma}_{min,b}$, $\bar{\sigma}_{j,b}$, $\bar{\sigma}_{w,b}$ and $\bar{d}_{min,b}$, referred to as the benchmark parameters, denoted with the subscript 'b' – see Fig. 22(b). Note that the parameters $\bar{\sigma}_{tip,b}$, $\bar{\sigma}_{min,b}$, $\bar{\sigma}_{j,b}$ and $\bar{\sigma}_{w,b}$ are stresses normalised by the yield stress

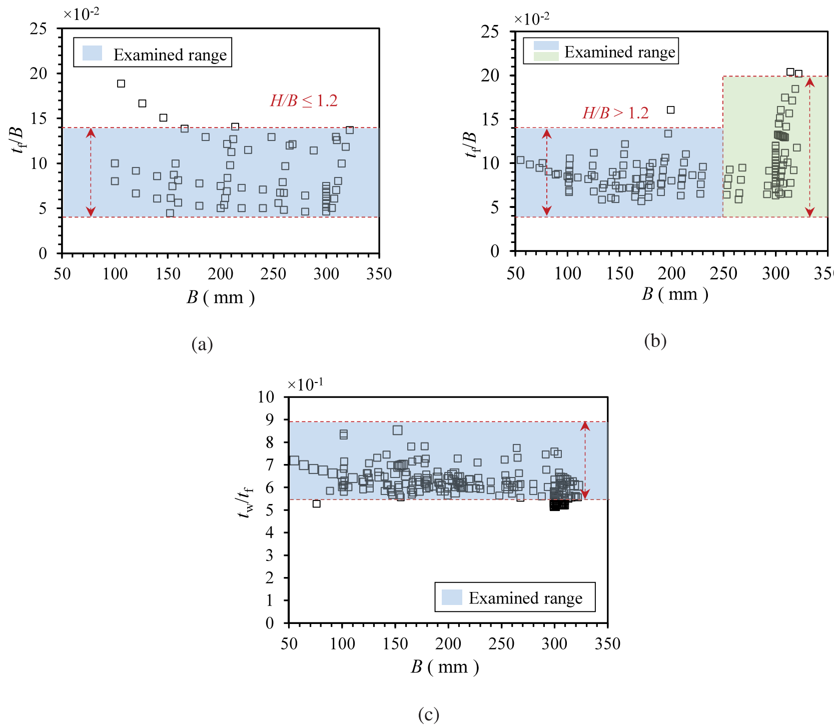

Fig. 20. Variation of ratios: (a) t_f/B when $H/B \leq 1.2$, (b) t_f/B when $H/B > 1.2$ and (c) t_w/t_f with flange width B for UC, UB, IPE and HE sections with $B \leq 350$ mm.

Table 8
Process parameters assumed for the WAAM of W_B-type stiffeners.

Process parameters	Value
Wire grade	ER70S-6
Wire diameter (mm)	1.2
Voltage (V)	19
Current (A)	238
Travel speed (mm/s)	6
Wire feed rate (m/min)	7.4

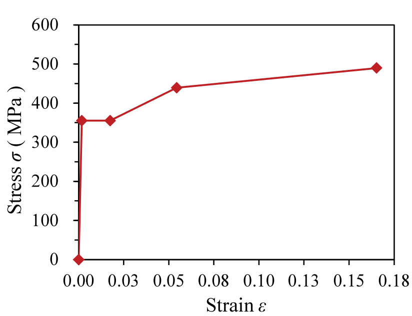

Fig. 21. Quad-linear stress–strain relationship assigned to simulated hot-rolled steel I-sections [57].

f_y, and the parameter $\bar{d}_{\mathrm{min,b}}$ is the distance from the flange tip to the point corresponding to the local minimum of stress within the flange, normalised by $B/2$. For each benchmark model examined in the parametric study, the benchmark parameters $\bar{\sigma}_{\mathrm{tip,b}}$ and $\bar{\sigma}_{\mathrm{min,b}}$ were first extracted from the FE results for each outstand portion of the two flanges, and then averaged to eliminate the underlying asymmetry (e.g., $\bar{\sigma}_{\mathrm{tip,b}}$ is taken as the average of the four normalised residual stress values at the flange tips). A similar procedure was also carried out for the determination of $\bar{\sigma}_{\mathrm{j,b}}$. Ordinary least squares regression analyses were subsequently conducted on these benchmark parameters, as described in the next section.

6.2. Regression analysis

The influence of the normalised areas — A_f/A_{wl} and A_b/A_{wl}, where A_f, A_b and A_{wl} are the cross-sectional areas of one flange, the base I-section, and a single weld line respectively, on the residual stresses in the studied WAAM-strengthened I-sections and, as such, on the five characteristic parameters presented in Section 6.1, is investigated herein through ordinary least squares regression analysis. In Figs. 23 and 24, the values of the five characteristic parameters extracted from the FE models in GroupA are plotted against A_f/A_{wl} and A_b/A_{wl} respectively. It is evident that the parameters $\bar{d}_{\mathrm{min,b}}$, $\bar{\sigma}_{\mathrm{j,b}}$ and $\bar{\sigma}_{\mathrm{w,b}}$ are strongly dependent on the two normalised areas, with $\bar{d}_{\mathrm{min,b}}$ having a stronger dependency on A_f/A_{wl}, and $\bar{\sigma}_{\mathrm{j,b}}$ and $\bar{\sigma}_{\mathrm{w,b}}$ having a stronger dependency on A_b/A_{wl}. As expected, the value of $\bar{d}_{\mathrm{min,b}}$ reduces with increasing normalised areas since the heat input from WAAM becomes increasingly localised. In Figs. 23(b) and 24(b), two distinct branches of data points can be observed, converging to 0.3 and 0.5, respectively, for high A_f/A_{wl} values. This is due to the residual stresses at the web-flange junction becoming less sensitive to the welding heat input as A_b increases, with the magnitude of $\bar{\sigma}_{\mathrm{j,b}}$ converging to the initial values of 0.3 for bare I-sections with $H/B > 1.2$, and of 0.5 for $H/B \leq 1.2$. A similar trend can be observed in Figs. 23(c) and 24(c) for $\bar{\sigma}_{\mathrm{w,b}}$, where the two branches converge to −0.3 and −0.5 for $H/B > 1.2$ and $H/B \leq 1.2$ respectively. The parameter $\bar{\sigma}_{\mathrm{tip,b}}$ shows a relatively stronger dependency on A_f/A_{wl}, with its magnitude gradually reducing with increasing values of A_f. Two branches of data points can be observed in both Figs. 23(e) and 24(e), which again corresponded to the aspect ratio and thus, the magnitudes of the initial residual stress of the I-sections. The data points in each branch converge with increasing values of A_f/A_{wl} and A_b/A_{wl}, since the initial residual stress pattern becomes less affected by the WAAM heat input.

Ordinary least squares regression analysis was employed to fit functions to the data points, thus correlating the residual stress parameters (except for $\bar{\sigma}_{\mathrm{min,b}}$) to A_f/A_{wl} and A_b/A_{wl}. The fitted curves are plotted in Figs. 23 and 24, with the additional subscript 'p' used to denote the fitted (predicted) parameters. The same process was also adopted for the FE models in Group B, and the characteristic parameters, except

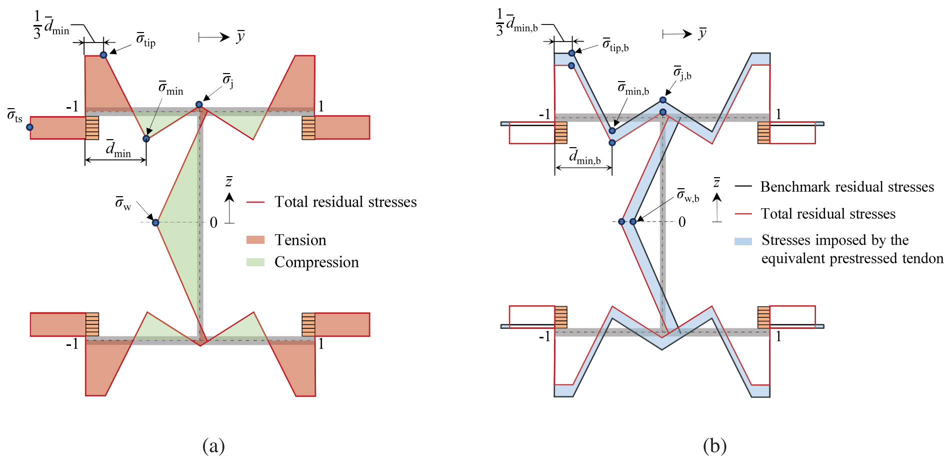

Fig. 22. General multi-linear residual stress pattern: (a) schematic illustration and (b) superposition of the benchmark distribution and the stresses imposed by the prestressed tendon (all parameters are normalised).

Table 9
Predictive expressions for the characteristic parameters used to define the benchmark residual stress pattern in WAAM-strengthened I-sections (Group A).

Characteristic parameters	Group A
$\bar{d}_{\mathrm{min,b,p}}$	$11(A_\mathrm{f}/A_\mathrm{wl})^{-0.7}$
$\bar{\sigma}_{\mathrm{j,b,p}}$	$\begin{cases} 0.5-40(A_\mathrm{b}/A_\mathrm{wl})^{-0.8} & (H/B \le 1.2) \\ 0.3-40(A_\mathrm{b}/A_\mathrm{wl})^{-0.9} & (H/B > 1.2) \end{cases}$
$\bar{\sigma}_{\mathrm{w,b,p}}$	$\begin{cases} -0.5-80(A_\mathrm{b}/A_\mathrm{wl})^{-1} & (H/B \le 1.2) \\ -0.3-60(A_\mathrm{b}/A_\mathrm{wl})^{-1} & (H/B > 1.2) \end{cases}$
$\bar{\sigma}_{\mathrm{tip,b,p}}$	$\frac{1}{1+\left(\frac{A_\mathrm{f}/A_\mathrm{wl}}{550}\right)^3}$
$\bar{\sigma}_{\mathrm{min,b,p}}$	$\frac{1}{\frac{1}{3}\bar{d}_{\mathrm{min,b,p}}-1}\left[\frac{(\bar{\sigma}_{\mathrm{w,b,p}}+\bar{\sigma}_{\mathrm{j,b,p}})(H-t_\mathrm{f})t_\mathrm{w}}{2Bt_\mathrm{f}}+\frac{4}{3}\bar{\sigma}_{\mathrm{tip,b,p}}\bar{d}_{\mathrm{min,b,p}}+(1-\bar{d}_{\mathrm{min,b,p}})\bar{\sigma}_{\mathrm{j,b,p}}\right]$

Table 10
Predictive expressions for the characteristic parameters used to define the benchmark residual stress pattern in WAAM-strengthened I-sections (Group B).

Characteristic parameters	Group B
$\bar{d}_{\mathrm{min,b,p}}$	$3(A_\mathrm{f}/A_\mathrm{wl})^{-0.45}$
$\bar{\sigma}_{\mathrm{j,b,p}}$	$\begin{cases} 0.5-100(A_\mathrm{b}/A_\mathrm{wl})^{-1} & (H/B \le 1.2) \\ 0.3-100(A_\mathrm{b}/A_\mathrm{wl})^{-1} & (H/B > 1.2) \end{cases}$
$\bar{\sigma}_{\mathrm{w,b,p}}$	$\begin{cases} -0.5-80(A_\mathrm{b}/A_\mathrm{wl})^{-1} & (H/B \le 1.2) \\ -0.3-200(A_\mathrm{b}/A_\mathrm{wl})^{-1.2} & (H/B > 1.2) \end{cases}$
$\bar{\sigma}_{\mathrm{tip,b,p}}$	$\frac{1}{1+\left(\frac{A_\mathrm{f}/A_\mathrm{wl}}{450}\right)^3}$
$\bar{\sigma}_{\mathrm{min,b,p}}$	$\frac{1}{\frac{1}{3}\bar{d}_{\mathrm{min,b,p}}-1}\left[\frac{(\bar{\sigma}_{\mathrm{w,b,p}}+\bar{\sigma}_{\mathrm{j,b,p}})(H-t_\mathrm{f})t_\mathrm{w}}{2Bt_\mathrm{f}}+\frac{4}{3}\bar{\sigma}_{\mathrm{tip,b,p}}\bar{d}_{\mathrm{min,b,p}}+(1-\bar{d}_{\mathrm{min,b,p}})\bar{\sigma}_{\mathrm{j,b,p}}\right]$

$\bar{\sigma}_{\mathrm{min,b}}$, are plotted against either $A_\mathrm{f}/A_\mathrm{wl}$ or $A_\mathrm{b}/A_\mathrm{wl}$ in Fig. 25. The predictive expressions for Group A and Group B are summarised in Tables 9 and 10 respectively.

The mean values and coefficients of variation (COV) of $\bar{d}_{\mathrm{min,b}}/\bar{d}_{\mathrm{min,b,p}}$, $\bar{\sigma}_{\mathrm{w,b}}/\bar{\sigma}_{\mathrm{w,b,p}}$, $\bar{\sigma}_{\mathrm{tip,b}}/\bar{\sigma}_{\mathrm{tip,b,p}}$ and $(\bar{\sigma}_{\mathrm{j,b}}-\bar{\sigma}_{\mathrm{j,b,p}})$, as shown in Table 11, were used to assess the accuracy of the regression models. Note that, the parameter $(\bar{\sigma}_{\mathrm{j,b}}-\bar{\sigma}_{\mathrm{j,b,p}})$ was employed instead of $\bar{\sigma}_{\mathrm{j,b}}/\bar{\sigma}_{\mathrm{j,b,p}}$, due to $\bar{\sigma}_{\mathrm{j,b}}$ often having values close to zero. Overall, good predictions were yielded by the regression models.

Regarding the parameter $\bar{\sigma}_{\mathrm{min,b}}$, this can be determined from Eq. (13) (also shown in Tables 9 and 10), which was derived based on cross-section equilibrium, by setting the integral of the residual stress over the cross-section equal to zero. Note that the stresses in the single-layer WAAM stiffeners are ignored in the integration, since their areas are trivial compared to that of the base section.

Table 11
Assessment of accuracy of predictive expressions for characteristic parameters for benchmark residual stress distributions.

Model group		$\bar{d}_{\mathrm{min,b}}/\bar{d}_{\mathrm{min,b,p}}$	$\bar{\sigma}_{\mathrm{w,b}}/\bar{\sigma}_{\mathrm{w,b,p}}$	$\bar{\sigma}_{\mathrm{tip,b}}/\bar{\sigma}_{\mathrm{tip,b,p}}$	$\bar{\sigma}_{\mathrm{j,b}}-\bar{\sigma}_{\mathrm{j,b,p}}$
A	Mean	1.22	0.98	1.14	−0.025
	COV	0.13	0.08	0.14	–
B	Mean	1.00	1.03	1.19	0.003
	COV	0.10	0.02	0.20	–

$$\bar{\sigma}_{\mathrm{min,b,p}}=\frac{1}{\frac{1}{3}\bar{d}_{\mathrm{min,b,p}}-1}\left[\frac{(\bar{\sigma}_{\mathrm{w,b,p}}+\bar{\sigma}_{\mathrm{j,b,p}})(H-t_\mathrm{f})t_\mathrm{w}}{2Bt_\mathrm{f}}+\frac{4}{3}\bar{\sigma}_{\mathrm{tip,b,p}}\bar{d}_{\mathrm{min,b,p}}+(1-\bar{d}_{\mathrm{min,b,p}})\bar{\sigma}_{\mathrm{j,b,p}}\right] \tag{13}$$

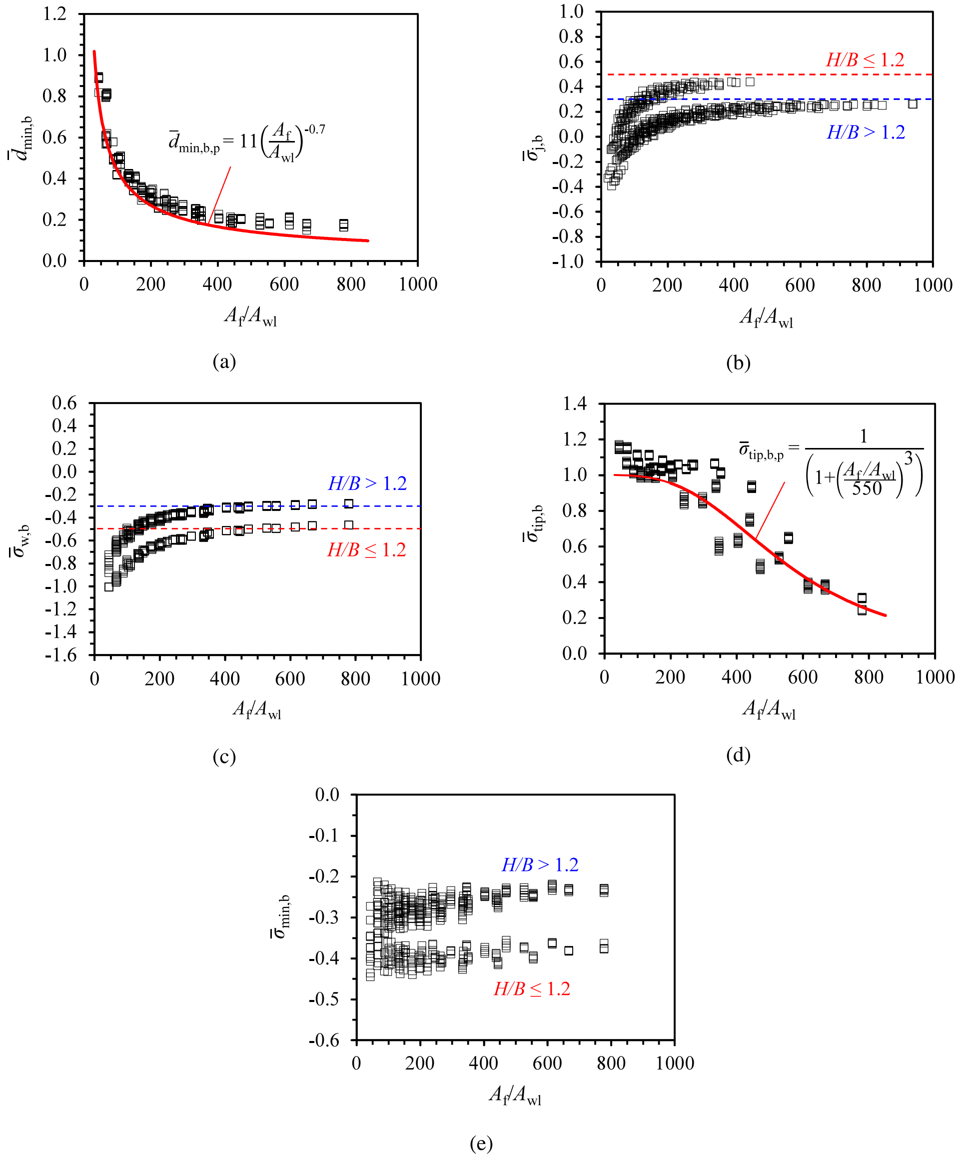

Fig. 23. Variation of the characteristic parameters with A_f/A_{wl} (Group A).

It should be mentioned that the analytical expressions given in Tables 9, 10 and Eq. (13) are for the benchmark members only; therefore, the residual stress distribution defined by these expressions is named as benchmark distributions herein.

6.3. Summary of predictive model and model validation

To allow for multi-layer WAAM stiffeners, the benchmark distributions, as given by the analytical expressions in Tables 9, 10 and Eq. (13), are modified using the equivalent prestressed tendon approach described in Section 4.1. The compressive stress induced by the prestressing effect from the additional weld layers, given by Eqs. (9) and (12), is superposed onto the benchmark distribution to obtain the final residual stress distribution in a WAAM-strengthened I-section. The predictive expressions (with the subscript 'p' omitted for clarity) used to define the final residual stress distribution are given in Tables 12 and 13 for WAAM-strengthened I-sections with 100 mm ≤ B ≤ 250 mm and with 250 mm ≤ B ≤ 350 mm respectively, where $f_{y,b}$ and $f_{y,w}$ are the yield stresses of the base hot-rolled steel and the WAAM steel respectively, and σ_{ts} is the residual stress in the WAAM tip stiffeners. Comparisons between the results determined from the modified predictive model and the results for the four specimens (one experimental and three numerical) listed in Table 14 are plotted in Fig. 26. Note that for the FE analyses of Cases 2–4, the S355 quad-linear stress–strain model [57] and the semi-static method were employed. Good agreement between the predicted results and those derived from the experiment and numerical simulations can be observed. For the examined WAAM-strengthened I-sections, the values of the benchmark parameters, obtained using the predictive expressions given in Tables 9 and 10, as well as the stresses imposed by the equivalent prestressed tendon — $\bar{\sigma}_{c,b}$ and $\bar{\sigma}_{c,w}$ (normalised by the yield stress f_y), as calculated using Eqs. (9) and (10), are summarised in Table 15. It should be mentioned that, although the current parametric study and the subsequent derivation of the predictive expressions are implemented based on certain sets of process parameters, a preliminary investigation has shown that the residual stress distributions in the WAAM-strengthened I-section members are relatively insensitive to changes in the process parameters, therefore indicating the general applicability of the established predictive model. Care should be taken however in applying

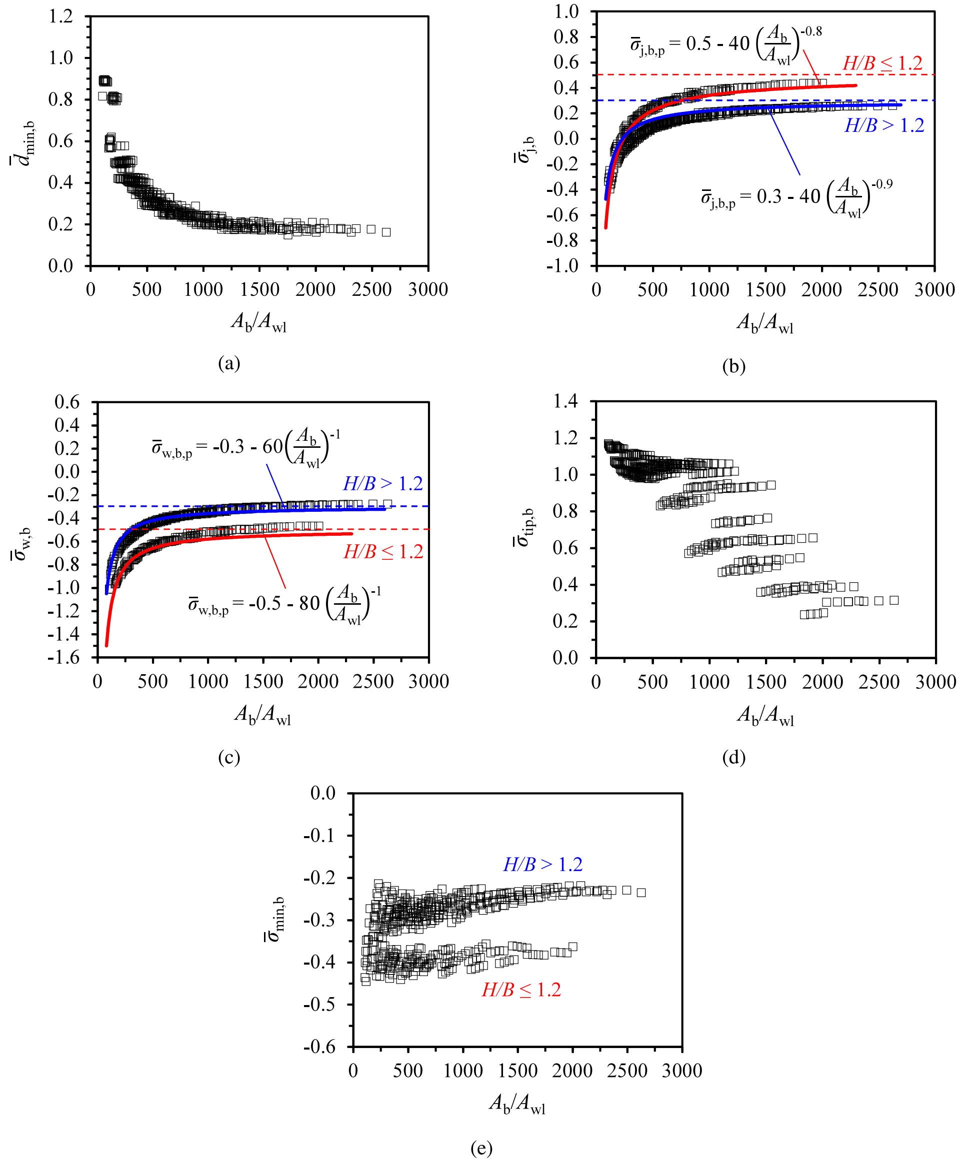

Fig. 24. Variation of the characteristic parameters with A_b/A_{wl} (Group A).

the model to cases where the energy input, the I-section and weld geometries or the manufacturing (printing) strategy differ substantially from those employed in the current study.

7. Conclusions

The magnitude and distribution of residual stresses in hot-rolled steel I-sections strengthened through the addition of WAAM stiffeners at the flange tips have been studied in the present paper. Two alternative FE modelling methods (the transient and the semi-static method) were employed and validated against experimental results [24], with the semi-static method found to save 98% computational power over the transient method, with no significant loss of accuracy. A hybrid numerical–analytical approach was further developed based on a proposed equivalent prestressed tendon method, which further improved the computational efficiency, while retaining good accuracy. It was found that the original underlying residual stress pattern in conventional hot-rolled I-sections is effectively reversed by the heat input from WAAM, with tensile residual stresses developing within the WAAM stiffeners and the flange tips, and with the magnitude of the residual stresses in other cross-section regions changing relative to their initial values to satisfy cross-section equilibrium. Following a comprehensive parametric study, a predictive model for the residual stress distribution in WAAM-strengthened I-sections, characterised by 5 key parameters, was established. The devised predictive residual stress model, which is suitable for incorporation into numerical simulations of WAAM-strengthened I-section members, can be applied to a wide range of standard hot-rolled I-section profiles, and has been shown to provide accurate results. Finally, the residual stresses in the WAAM-strengthened I-sections were found to be relatively insensitive to the changes in the process parameters, indicating that the established predictive model has a relatively general applicability and is suitable for practical applications where the process parameters are not substantially different from those examined in the current study.

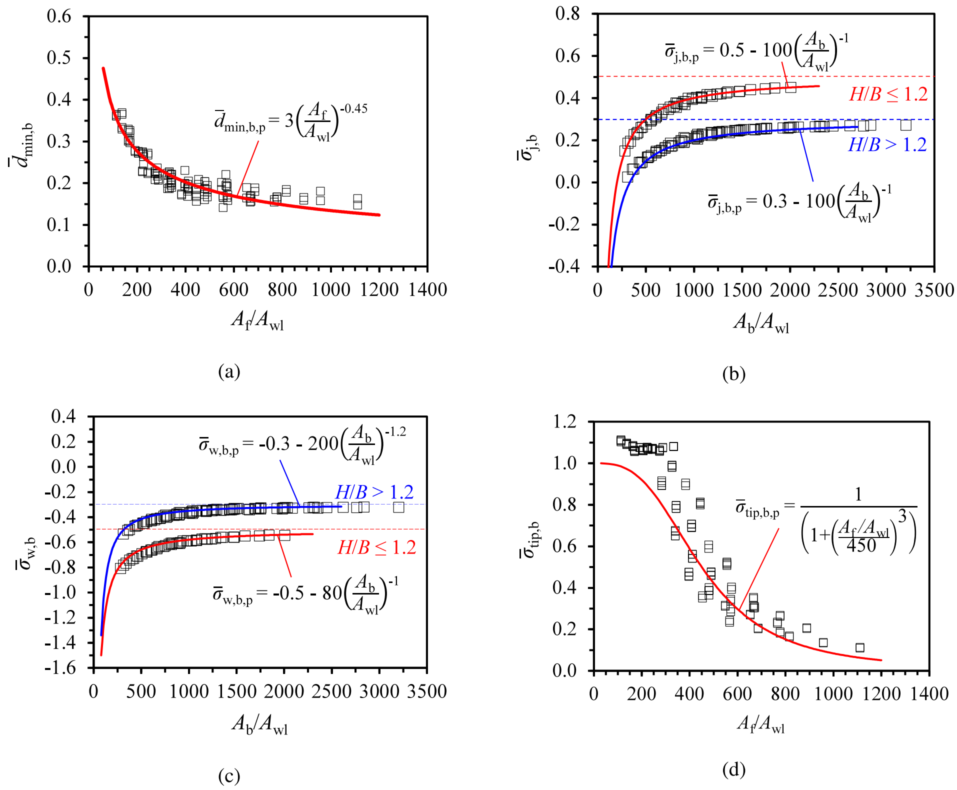

Fig. 25. Variation of the characteristic parameters with A_f/A_{wl} or A_b/A_{wl} (Group B).

Table 12
Summary of predictive model expressions for the final residual stress distribution in WAAM-strengthened I-sections with 100 mm $\leq B \leq$ 250 mm and W_A-type stiffeners (all parameters are unnormalised).

Parameters	Predictive expressions
d_{min}	$\frac{11}{2}B(A_f/A_{wl})^{-0.7}$
σ_{tip}	$\frac{f_{y,b}}{1+\left(\frac{A_f/A_{wl}}{550}\right)^3} + \sigma_{c,b}$
σ_j	$\begin{cases} [0.5 - 40(A_b/A_{wl})^{-0.8}]f_{y,b} + \sigma_{c,b} & (H/B \leq 1.2) \\ [0.3 - 40(A_b/A_{wl})^{-0.9}]f_{y,b} + \sigma_{c,b} & (H/B > 1.2) \end{cases}$
σ_w	$\begin{cases} -[0.5 + 80(A_b/A_{wl})^{-1}]f_{y,b} + \sigma_{c,b} & (H/B \leq 1.2) \\ -[0.3 + 60(A_b/A_{wl})^{-1}]f_{y,b} + \sigma_{c,b} & (H/B > 1.2) \end{cases}$
σ_{min}	$\frac{1}{\frac{2}{3}d_{min} - B}\left[\frac{(\sigma_w+\sigma_j)(H-t_f)t_w}{2t_f} + \frac{4nA_{wl}\sigma_{ts}}{t_f} + \frac{8}{3}\sigma_{tip}d_{min} + (B - 2d_{min})\sigma_j\right]$
σ_{ts}	$f_{y,w} + \sigma_{c,w}$

$\sigma_{c,b} = \frac{-E_b f_{y,w} 4(n-1)A_{wl}}{E_b A_b + 4nE_w A_{wl}}$, $\sigma_{c,w} = \frac{-E_w f_{y,w} 4(n-1)A_{wl}}{E_b A_b + 4nE_w A_{wl}}$

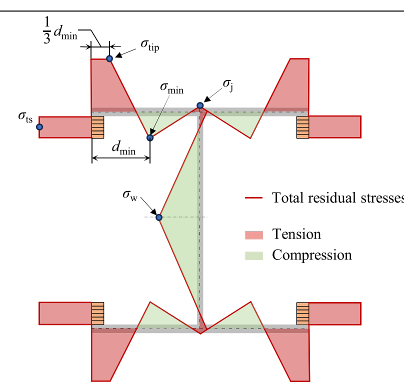

CRediT authorship contribution statement

Jiachi Yang: Writing – original draft, Validation, Methodology, Investigation, Formal analysis, Conceptualization. **Pinelopi Kyvelou:** Writing – review & editing, Validation, Methodology, Investigation. **M. Ahmer Wadee:** Writing – review & editing, Supervision, Resources, Project administration, Methodology, Funding acquisition. **Leroy Gardner:** Writing – original draft, Validation, Supervision, Project administration, Funding acquisition, Conceptualization.

Declaration of competing interest

The author is an Editorial Board Member/Editor-in-Chief/Associate Editor/Guest Editor for *Structures* and was not involved in the editorial review or the decision to publish this article.

Co-author: Leroy Gardner is the Editor-in-Chief of Structures

Co-author: M Ahmer Wadee is an Editorial Board Member of Structures

Acknowledgements

The authors wish to express their gratitude to Steelo Ltd for the manufacturing of the specimens used in this study. The authors are also thankful to Dr Ruizhi Zhang for providing the micrograph of the WAAM stiffeners. We would like to thank Imperial College London for the financial support provided through the Civil Engineering Skempton scholarship for the lead author.

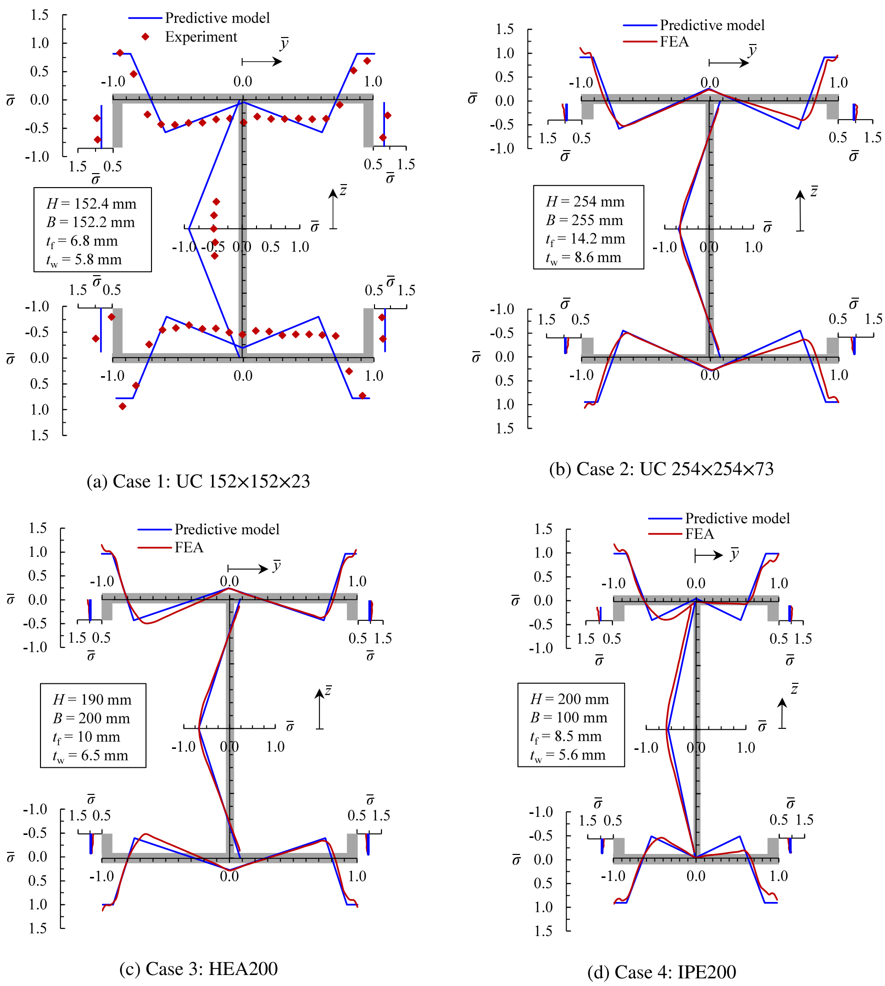

Fig. 26. Validation of proposed predictive model: (a) Case 1, (b) Case 2, (c) Case 3 and (d) Case 4 (as per Table 14).

Table 13
Summary of predictive model expressions for the final residual stress distribution in WAAM-strengthened I-sections with 250 mm ≤ B ≤ 350 mm and W_B-type stiffeners (all parameters are unnormalised).

Parameters	Predictive expressions
d_{min}	$\frac{3}{2}B(A_f/A_{wl})^{-0.45}$
σ_{tip}	$\frac{f_{y,b}}{1+\left(\frac{A_f/A_{wl}}{450}\right)^3}+\sigma_{c,b}$
σ_j	$\begin{cases}[0.5-100(A_b/A_{wl})^{-1}]f_{y,b}+\sigma_{c,b} & (H/B\le 1.2)\\ [0.3-100(A_b/A_{wl})^{-1}]f_{y,b}+\sigma_{c,b} & (H/B>1.2)\end{cases}$
σ_w	$\begin{cases}-[0.5+80(A_b/A_{wl})^{-1}]f_{y,b}+\sigma_{c,b} & (H/B\le 1.2)\\ -[0.3+200(A_b/A_{wl})^{-1.2}]f_{y,b}+\sigma_{c,b} & (H/B>1.2)\end{cases}$
σ_{min}	$\frac{1}{\frac{2}{3}d_{min}-B}\left[\frac{(\sigma_w+\sigma_j)(H-t_f)t_w}{2t_f}+\frac{4nA_{wl}\sigma_{ts}}{t_f}+\frac{8}{3}\sigma_{tip}d_{min}+(B-2d_{min})\sigma_j\right]$
σ_{ts}	$f_{y,w}+\sigma_{c,w}$

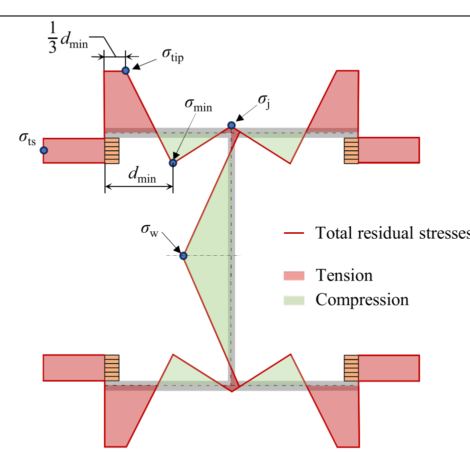

$\sigma_{c,b}=\frac{-E_b f_{y,w}4(n-1)A_{wl}}{E_b A_b+4nE_w A_{wl}}$, $\sigma_{c,w}=\frac{-E_w f_{y,w}4(n-1)A_{wl}}{E_b A_b+4nE_w A_{wl}}$

Table 14
Cases used for validation of the proposed predictive model.

Case	Base I-section	Weld type	Number of weld layers in each stiffener	Initial residual stress pattern	Result type
1	UC 152 × 152 × 23	W_A	18	Measured	Experimental
2	UC 254 × 254 × 73	W_B	6	ECCS	Numerical
3	HEA200	W_A	6	ECCS	Numerical
4	IPE200	W_A	6	ECCS	Numerical

Table 15
Characteristic parameters of the benchmark residual stress distributions, and the stresses imposed by the equivalent prestressed tendon, for the examined WAAM-strengthened I-sections.

Case	Base I-section	$\bar{d}_{min,b,p}$	$\bar{\sigma}_{j,b,p}$	$\bar{\sigma}_{w,b,p}$	$\bar{\sigma}_{tip,b,p}$	$\bar{\sigma}_{min,b,p}$	$\bar{\sigma}_{c,b}$	$\bar{\sigma}_{c,w}$
1	UC 152 × 152 × 23	0.40	0.13	−0.75	0.99	−0.41	−0.17	−0.17
2	UC 254 × 254 × 73	0.30	0.30	−0.64	0.95	−0.55	−0.05	−0.05
3	HEA200	0.25	0.27	−0.64	0.94	−0.44	−0.03	−0.03
4	IPE200	0.46	0.05	−0.50	0.99	−0.41	−0.06	−0.06

References

[1] Gardner L. Metal additive manufacturing in structural engineering – review, advances, opportunities and outlook. Structures 2023;47:2178–93.
[2] Meng X, Weber B, Nitawaki M, Gardner L. Optimisation and testing of wire arc additively manufactured steel stub columns. Thin-Walled Struct 2023;189:110857.
[3] Williams SW, Martina F, Addison AC, Ding J, Pardal G, Colegrove P. Wire + arc additive manufacturing. Mater Sci Technol 2016;32(7):641–7.
[4] Ye J, Kyvelou P, Gilardi F, Lu H, Gilbert M, Gardner L. An end-to-end framework for the additive manufacture of optimized tubular structures. IEEE Access 2021;9:165476–89.
[5] Laghi V, Palermo M, Gasparini G, Girelli VA, Trombetti T. Experimental results for structural design of wire-and-arc additive manufactured stainless steel members. J Constr Steel Res 2020;167:105858.
[6] Shah IH, Hadjipantelis N, Walter L, Myers RJ, Gardner L. Environmental life cycle assessment of wire arc additively manufactured steel structural components. J Clean Prod 2023;389:136071.
[7] Kyvelou P, Spinasa A, Gardner L. Testing and analysis of optimized wire arc additively manufactured steel trusses. J Struct Eng 2024;150(3):04024008a.
[8] Wang Z, Hou Y, Huang C, Han Q, Zong L, Chen M, Deng K, Gardner L. Experimental study and constitutive modelling of wire arc additively manufactured steel under cyclic loading. J Constr Steel Res 2024;213:108420.
[9] Huang C, Kyvelou P, Gardner L. Stress–strain curves for wire arc additively manufactured steels. Eng Struct 2023;279:115628.
[10] Waldschmitt B, Costanzi CB, Knaack U, Lange J. 3D printing of column structures for architectural applications. Archit Struct Constr 2022;2(4):565–74.
[11] Hadjipantelis N, Weber B, Buchanan C, Gardner L. Description of anisotropic material response of wire and arc additively manufactured thin-walled stainless steel elements. Thin-Walled Struct 2022;171:108634.
[12] Liu Y, Gannon L. Experimental behavior and strength of steel beams strengthened while under load. J Constr Steel Res 2009;65(6):1346–54a.
[13] Liu Y, Gannon L. Finite element study of steel beams reinforced while under load. Eng Struct 2009;31(11):2630–42b.
[14] Zhao X, Zhang L. State-of-the-art review on FRP strengthened steel structures. Eng Struct 2007;29(8):1808–23.
[15] Izadi M, Motavalli M, Ghafoori E. Iron-based shape memory alloy Fe-SMA for fatigue strengthening of cracked steel bridge connections. Constr Build Mater 2019;227:116800.
[16] Izadi M, Motavalli M, Ghafoori E. Thermally-activated shape memory alloys for retrofitting bridge double-angle connections. Eng Struct 2021;245:112827.
[17] Osofero AI, Wadee MA, Gardner L. Experimental study of critical and post-buckling behaviour of prestressed stayed columns. J Constr Steel Res 2012;79:226–41.
[18] Gardner L, Li J, Meng X, Huang C, Kyvelou P. I-section steel columns strengthened by wire arc additive manufacturing – concept and experiments. Eng Struct 2024;306:117763.
[19] Withers PJ, Bhadeshia HKDH. Residual stress. Part 2 – nature and origins. Mater Sci Technol 2001;17(4):366–75.
[20] Rossini NS, Dassisti M, Benyounis KY, Olabi AG. Methods of measuring residual stresses in components. Mater Des 2012;35:572–88.
[21] Tebedge N, Alpsten G, Tall L. Residual-stress measurement by the sectioning method. Exp Mech 1973;13(2):88–96.
[22] Gardner L, Bu Y, Theofanous M. Laser-welded stainless steel I-sections: Residual stress measurements and column buckling tests. Eng Struct 2016;127:536–48.
[23] Yuan HX, Wang YQ, Shi YJ, Gardner L. Stub column tests on stainless steel built-up sections. Thin-Walled Struct 2014;83:103–14a.
[24] Kyvelou P, Huang C, Li J, Gardner L. Residual stresses in steel I-sections strengthened by wire arc additive manufacturing. Structures 2024;60:105828b.
[25] Lindgren LE. Numerical modelling of welding. Comput Methods Appl Mech Engrg 2006;195(48–49):6710–36.
[26] Kucukler M, Xing Z, Gardner L. Behaviour and design of stainless steel isection columns in fire. J Constr Steel Res 2020;165:105890.
[27] Wang HX, Yuan an YQ, Gardner L, Shi YJ. Local-overall interactive buckling of welded stainless steel box section compression members. Eng Struct 2014;67:62–76b.
[28] Meng X, Gardner L. Cross-sectional behaviour of cold-formed high strength steel circular hollow sections. Thin-Walled Struct 2020;156:106822a.
[29] Liang Y, Zhao O, Long YL, Gardner L. Stainless steel channel sections under combined loading – part 1: Experimental study and numerical modelling. J Constr Steel Res 2019;152:154–61.
[30] EN ISO 6892-1: metallic materials – tensile testing – part 1: method of test at room temperature. Brussels: European Committee for Standardization (CEN); 2016.
[31] Ding J, Colegrove P, Mehnen J, Ganguly S, Almeida PMS, Wang F, Williams S. Thermo-mechanical analysis of wire and arc additive layer manufacturing process on large multi-layer parts. Comput Mater Sci 2011;50(12):3315–22.
[32] Ghosh S, Choi J. Three-dimensional transient finite element analysis for residual stresses in the laser aided direct metal/material deposition process. J Laser Appl 2005;17(3):144–58.
[33] Liu X, Chung K. Experimental and numerical investigation into temperature histories and residual stress distributions of high strength steel S690 welded H-sections. Eng Struct 2018;165:396–411.
[34] Alrumayh AA. Residual stresses analysis of 3d printed plate by using wire arc additive manufacturing - WAAM (Master's thesis), Lehigh University; 2018.
[35] Zubairuddin M, Albert SK, Vasudevan M, Mahadevan S, Chaudhari V, Suri VK. Numerical simulation of multi-pass GTA welding of grade 91 steel. J Manuf Process 2017;27:87–97.
[36] Dewees DJ. Comparison of 2D and 3D welding simulations of a simple plate. In: Volume 2: computer technology and bolted joints. Toronto, Ontario, Canada: American Society of Mechanical Engineers; 2012, p. 273–81.
[37] Huang H, Ma N, Chen J, Feng Z, Murakawa H. Toward large-scale simulation of residual stress and distortion in wire and arc additive manufacturing. Addit Manuf 2020;34:101248.
[38] Goldak JA, Akhlaghi M. Computational welding mechanics. New York: Springer; 2005.
[39] Abaqus analysis user's manual. Version 2023 ed.. Providence, RI: Dassault Systems; 2023.
[40] Eurocode 3: design of steel structures. part 1-2: general rules - structural fire design. Brussels: European Committee for Standardization; 2022.
[41] Ding J. Thermo-mechanical analysis of wire and arc additive manufacturing process (Ph.D. thesis), Cranfield: Cranfield University; 2012.
[42] Zhu XK, Chao YJ. Effects of temperature-dependent material properties on welding simulation. Comput Struct 2002;80(11):967–76.
[43] Lindgren LE. Computational welding mechanics: thermomechanical and microstructural simulations. publ ed.. Vol. 1, Cambridge: Woodhead publishing in materials. Woodhead Publ.; 2007.
[44] Shanghvi JY, Michaleris P. Thermo-elasto-plastic finite element analysis of quasi-state processes in Eulerian reference frames. Internat J Numer Methods Engrg 2002;53(7):1533–56.
[45] Goldak J, Chakravarti A, Bibby M. A new finite element model for welding heat sources. Metall Trans B 1984;15(2):299–305.
[46] Young BW. Residual stresses in hot rolled members. In: IABSE reports of the working commissions. 1975, p. 23–5.
[47] Ultimate limit state calculations of sway frames with rigid joints. Brussels: European Convention for Constructional Steelwork (ECCS); 1984.
[48] Nethercot DA. Residual stresses and their influence upon the lateral buckling of rolled steel beams. Struct Eng 1974;52(3):89–96.

[49] Kucukler M, Gardner L, Macorini L. Lateral–torsional buckling assessment of steel beams through a stiffness reduction method. J Constr Steel Res 2015;109:87–100.
[50] White JD. Longitudinal stresses in a member containing non-interacting welds. CUED technical report, CUED/C-Struct/TR. 58, 1977.
[51] Grams MR, Mendez PF. A general expression for the welding tendon force. J Manuf Sci Eng 2021;143(12):121002.
[52] Grams MR. Predictive expressions for residual stress and distortion in welding and related thermal processes (Ph.D. thesis), University of Alberta; 2021.
[53] Hadjipantelis N, Gardner L, Wadee MA. Prestressed cold-formed steel beams: Concept and mechanical behaviour. Eng Struct 2018;172:1057–72.
[54] Meng X, Gardner L. Behavior and design of normal and high strength steel SHS and RHS columns. J Struct Eng 2020;146(11):04020227b.
[55] Gardner L, Yun X, Walport F. The continuous strength method – review and outlook. Eng Struct 2023;275:114924.
[56] Yun X, Gardner L, Boissonnade N. The continuous strength method for the design of hot-rolled steel cross-sections. Eng Struct 2018;157:179–91.
[57] Yun X, Gardner L. Stress–strain curves for hot-rolled steels. J Constr Steel Res 2017;133:36–46.
[58] Eurocode 3: design of steel structures. Part 1-1: general rules and rules for buildings. Brussels: European Committee for Standardization; 2022.